Simple kinetic Monte Carlo models for dissolution pitting induced by crystal defects

Paul Meakin[1] and Kevin M. Rosso[2,a)]
[1]*Center for Advanced Modeling and Simulation, Idaho National Laboratory, P.O. Box 1625, Mail Stop 2211, Idaho Falls, Idaho 83415-2211, USA*
[2]*Pacific Northwest National Laboratory, P.O. Box 999, Mail Stop K8-96, Richland, Washington 99354, USA*

(Received 29 July 2008; accepted 15 October 2008; published online 25 November 2008)

The solid-on-solid kinetic Monte Carlo model of Lasaga and Blum [Geochim. Cosmochim. Acta **50**, 2363 (1986)] for dislocation-controlled etch-pit growth has been extended to the growth of etch pits under the control of multiple dislocations and point defects. This required the development of algorithms that are $O(10^3)-O(10^4)$ times faster than primitive kinetic Monte Carlo models for surfaces with areas in the range of $1024\times1024-4096\times4096$ lattice sites. Simulations with multiple line defects indicate that the surface morphology coarsens with increasing time and that the coarsening is more pronounced for large bond-breaking activation energies. For small bond breaking activation energies dissolution enhanced by line defects perpendicular to the dissolving surface results in pits with steep sides terminated by deep narrow hollow tubes (nanopipes). Larger bond breaking activation energies lead to shallow pits without deep nanopipes, and if the bond breaking activation energy is large enough, step flow is the primary dissolution mechanism, and pit formation is suppressed. Simplified models that neglect the far field strain energy density but include either a rapidly dissolving core or an initially empty core lead to results that are qualitatively similar to those obtained using models that include the effects of the far field stress and strain. Simulations with a regular array of line defects show that microscopic random thermal fluctuations play an important role in the coarsening process. © *2008 American Institute of Physics*.
[DOI: 10.1063/1.3021478]

INTRODUCTION

Mineral dissolution plays an important role in numerous geological processes over a wide range of time and length scales. It provides a source of dissolved ions that can form new mineral phases, react with atmospheric gasses, and provide nutrients in soils and surface water. The dissolution of minerals and their precipitation, or the precipitation of new minerals, plays an important role in the rheological behavior of the Earth's crust,[1,2] and these processes are also important in processes such as oil recovery, the formation of commercially important mineral deposits, and the behavior of metallic and radioactive contaminants in the subsurface. The formation of etch pits is prominent in most mineral dissolution processes,[3] and it is widely believed that accelerated dissolution in the vicinity of dislocations is an important, often dominant, process during mineral dissolution.[4] Mineral dissolution by carbonic acid and the precipitation of carbonates by the reaction of dissolved metals and carbonate play a dominant role in the long time scale carbon cycle,[5] and the dissolution and precipitation of minerals also play an important role in the assessment of proposed carbon sequestration processes and their potential environmental impact.[6,7]

The formation of etch pits is important in other substances,[8–11] and etching is still being used to investigate defects in technologically important materials. In addition, the role that dislocation induced etch pits play in the control of surface morphology in electronic and optical devices is also an active area of research with important applications.[12,13] There is also evidence that etch pits may play an important role in biological mineralization and demineralization processes.

The formation of distinct pits is a common occurrence during the dissolution of low index crystal surfaces, and in many cases it has been demonstrated that the growth of etch pits is associated with defects in the crystal structure. In particular, the nucleation of an etch pit at the point where line defects (dislocations) emerge from crystal surfaces has been used to study the distribution[14–17] and behavior[18] of dislocations and to determine their density. Much of the work on crystal dissolution has traditionally been focused on the evolution of surface morphology in the immediate vicinity of isolated defects.[19–23] However, the disordered spatial distribution of defects (particularly extended defects) in naturally occurring and synthetic crystals leads to the development of complex surface morphologies that cannot easily be understood in terms of the geometry of etch pits formed in close proximity to isolated defects.[24–26] Consequently, it is important to develop methods that can be used to simulate the simultaneous growth of interacting etch pits associated with a large number of diverse defects. The objective of this work is to create a basic framework for such simulations using a simple cubic crystal lattice as an example. To achieve this objective, it was necessary to develop kinetic Monte Carlo

[a)]Electronic mail: kevin.rosso@pnl.gov.

 © 2008 American Institute of Physics

Author complimentary copy. Redistribution subject to AIP license or copyright, see http://jcp.aip.org/jcp/copyright.jsp

models that are efficient for lattices that are large enough to contain a large number of defects at realistic densities.

The rate of mineral dissolution may be limited by either transport processes or by reaction processes. In this paper, we focus on reaction-limited dissolution processes, which are dominant when the rates of surface reaction are slow and/or diffusion distances are small. Diffusion distances can be reduced by using rapid flow rates to reduce the thickness of the fluid boundary layer, but the formation of very rough surfaces and/or deep pits may lead to a crossover from reaction-limited dissolution at early times to transport-limited behavior at later times. These effects are not considered in this work.

The dissolution process was simulated using a three-dimensional, cubic lattice, kinetic Monte Carlo model, very similar to that used by Lasaga and co-workers.[19,22,23] In this model, each site on the cubic lattice is considered to be occupied by either fluid or solid. The model does not attempt to simulate the details of surface reaction processes. Instead, the dissolution of the solid is represented by the conversion of a solid site at the surface (a solid site with one or more neighboring fluid sites) into a fluid site. A "solid-on-solid" model, which restricts the dissolution to the highest occupied solid site in each column of the lattice, was used. The solid-on-solid approximation, which prevents overhangs from forming and simplifies the "book keeping" involved in the simulations, has been used extensively in kinetic Monte Carlo models for dissolution and growth[27–30] including models for pit growth.[31] In the kinetic Monte Carlo model, it is assumed that the rate of dissolution of a solid site on the top of a column of solid sites is given by

$$R_{\text{diss}} = Ae^{-(E_a/k_BT)}, \tag{1}$$

where A is the frequency factor, E_a is the activation energy for removal of that site, k_B is the Boltzmann constant, and T is the absolute temperature. As is common in physics applications, energy units of k_BT were used in this work. The activation energy that must be overcome to remove (dissolve) a solid site is assumed to be proportional to the number of occupied, or solid, nearest neighbors (the coordination number), n. Under these conditions, Eq. (1) can be replaced by[29]

$$R_{\text{diss}} = Ae^{-(nE_b)}. \tag{2}$$

The activation free energy for the dissolution of typical minerals lies in the range of $30 < E_a < 75$ kJ/mole (Refs. 32–34) and $k_BT = 2.328$ kJ/mole at 280 K. Consequently, $12 < E_a < 33$ in units of k_BT, and since an average of three bonds is broken during a dissolution event simulated using a simple cubic lattice model (in addition, the most probable dissolution event is the removal of a three-coordinate site at a kink at the edge of a terrace), it is reasonable to use values in the range of $4 < E_b < 11$ for the "bond-breaking activation energy." In most of the simulations described later in this paper, bond-breaking activation energies toward the lower end of this range ($3 < E_b < 8$) were used. Bond-breaking activation energies below the range characteristic of the dissolution of most minerals under natural conditions could be relevant to dissolution under more chemically aggressive conditions in the laboratory and the dissolution of some synthetic materials. The bond breaking activation energies are much smaller than the energies required to break chemical bonds. The reason for this is that dissolution is very different from removing an atom from a mineral surface in a vacuum. In dissolution processes, much of the energy required to remove material from a mineral surface is compensated for by solvation of the dissolved ions.

In a strained solid, the rate of dissolution is enhanced because the activation energy is reduced, and this is important in processes such as pressure solution creep.[35–38] It is intuitively obvious that the strain energy released by removal of a site from the surface will increase with the site coordination number n, and, on average, three bonds are broken each time an occupied site is removed. If it is assumed that the activation energy is reduced by the strain energy released by dissolution, then the most simple assumption is that the activation energy is reduced by $n\upsilon\rho_E/3$, where υ is the volume represented by a lattice site and ρ_E is the strain energy density.[22] If these assumptions are accepted, then the rate of dissolution of a solid site is given by

$$R_{\text{diss}} = Ae^{-n(E_b - \upsilon\rho_E/3)}, \tag{3}$$

and this equation can be replaced by

$$R_{\text{diss}} = Ae^{-n(E_b - \rho_E/3)}, \tag{4}$$

if the lattice unit a is used as the unit of length ($\upsilon = a^3 = 1$).

There is no compelling reason to assume that the energy required to remove a site from an unstrained surface or the strain energy released by dissolution should be proportional to the coordination number n. Indeed, the effects of next-nearest-neighbor interactions (and longer range interactions) on the change in energy when a site is added to or removed from a surface in the absence of strain have been included in many Monte Carlo simulations[39,40] and the same approach could be used in the presence of strain. This work is concerned with non-material-specific generic behavior, and there is no reason to encumber (and slow down) the simulations with nonessential details. Additional details such as next-nearest neighbor interactions, a more complex lattice structure, and anisotropy will be added when this modeling approach is used to simulate the behavior observed in laboratory experiments.

The work described in this paper was focused on irreversible dissolution processes, and Eq. (4) is the basis for the Monte Carlo simulations. The fast kinetic Monte Carlo algorithms described below can be applied to simulations that include other processes such as growth of the surface and surface diffusion.

In order to use Eq. (4) in the Monte Carlo simulations, the bond-breaking activation energy is simply selected as a parameter in the model, but the energy density field $\rho_E(\mathbf{x})$ must be calculated. The energy density field associated with a single defect can be divided into two components: a far-field component at positions $\mathbf{x}$ at which the strain is small enough for the stress and strain to be linearly related to each other; and a core component near to the center, or center line, of the defect. The far field component can then be calculated using the well-established theory of linear elasticity, but this

Author complimentary copy. Redistribution subject to AIP license or copyright, see http://jcp.aip.org/jcp/copyright.jsp

far field component diverges as the center (or center line) of the defect is approached, and the theory of linear elasticity breaks down in this core region. The strain energy density in the core region cannot be obtained from the theory of linear elasticity, and it is usually estimated either by using an empirical cutoff function that prevents the stress/strain fields from diverging or by simply truncating the strain energy density at a threshold value of $\rho_E^{\max}$ (another parameter in the model). The radius of the core region depends on the structure and interatomic interactions in the crystal, and it is typically 0.5–2.5 times the magnitude of the Burgers vector.[41] In all of the simulations described in this paper, the Burgers vector **b** defining the far field displacement was assigned a magnitude of $|\mathbf{b}|=1$, in lattice units. Whether a cutoff function or a strain energy threshold was used, the radius of the core was well within the range of $0.5b \leqslant r_c \leqslant 2.5b$. If multiple defects are present, the stress and strain fields can be calculated by first summing the far field stress and strain fields associated with the individual defects using the theory of linear elasticity. The strain energy density can then calculated from these stress and strain fields, and a variety of procedures can be used to truncate the strain energy density in the highly deformed core regions.

If these ideas are accepted, then the main task is to compute the far field strain energy density field using the standard theory of linear elasticity.

Linear elasticity and elastic energy density

According to the theory of linear elasticity,[42] the elastic energy density is given by

$$\rho_E = \frac{1}{2}\sum_i \sum_j \varepsilon_{ij}\sigma_{ij} = \frac{1}{2}\boldsymbol{\varepsilon}:\boldsymbol{\sigma} = \frac{1}{2}\boldsymbol{\varepsilon}:\mathbf{C}:\boldsymbol{\varepsilon}, \tag{5}$$

where $\boldsymbol{\varepsilon}$ is the second rank strain tensor, $\boldsymbol{\sigma}$ is the second rank stress tensor, and **C** is the fourth rank elastic constant tensor. Equation (5) can be expressed in the form

$$\rho_E = \tfrac{1}{2}\boldsymbol{\varepsilon}' \cdot \boldsymbol{\sigma}' = \tfrac{1}{2}\boldsymbol{\varepsilon}' \cdot \mathbf{C}' \cdot \boldsymbol{\varepsilon}', \tag{6}$$

where $\boldsymbol{\sigma}'$ is a vector containing the 9 elements of $\boldsymbol{\sigma}$, $\boldsymbol{\varepsilon}'$ is a vector containing the 9 elements of $\boldsymbol{\varepsilon}$, and $\mathbf{C}'$ is a second rank tensor containing the 81 elements of **C**. Symmetry considerations allow Eqs. (5) and (6) to be reduced to

$$\rho_E = \tfrac{1}{2}\boldsymbol{\varepsilon}'' \cdot \boldsymbol{\sigma}'' = \tfrac{1}{2}\boldsymbol{\varepsilon}'' \cdot \mathbf{C}'' \cdot \boldsymbol{\varepsilon}'', \tag{7}$$

where $\boldsymbol{\sigma}''=[\sigma_{11},\sigma_{22},\sigma_{33},\sigma_{12},\sigma_{13},\sigma_{23}]$, $\boldsymbol{\varepsilon}''=[\varepsilon_{11},\varepsilon_{22},\varepsilon_{33},\gamma_{12},\gamma_{13},\gamma_{23}]$, and $\mathbf{C}''$ is a 6×6 second rank tensor containing elements of **C**. Here, $\gamma_{ij}=2\varepsilon_{ij}$ is the "engineering shear strain."

In the interest of simplicity, attention is confined to isotropic materials with elastic properties that can be defined by two elastic coefficients. Under these conditions, the tensor $\mathbf{C}''$ has the form

$$\mathbf{C}'' = \begin{bmatrix} \mathbf{A} & \mathbf{0} \\ \mathbf{0} & \mathbf{B} \end{bmatrix}, \tag{8}$$

where **B** is diagonal. In Eq. (8), **A** has the form

$$\begin{aligned}\mathbf{A} &= \begin{bmatrix} C''_{11} & C''_{12} & C''_{13} \\ C''_{21} & C''_{22} & C''_{23} \\ C''_{31} & C''_{32} & C''_{33} \end{bmatrix} \\ &= \begin{bmatrix} \lambda+2\mu & \lambda & \lambda \\ \lambda & \lambda+2\mu & \lambda \\ \lambda & \lambda & \lambda+2\mu \end{bmatrix} \\ &= \frac{Y}{(1+\nu)(1-2\nu)}\begin{bmatrix} 1-\nu & \nu & \nu \\ \nu & 1-\nu & \nu \\ \nu & \nu & 1-\nu \end{bmatrix},\end{aligned} \tag{9}$$

where λ and μ are the Lame coefficients. In Eq. (9), Y is Young's modulus and ν is the Poisson ratio. The matrix **B** is diagonal and all diagonal elements of **B** are equal to the Lame coefficient μ, which is often given the symbol G, and referred to as the shear modulus. For an isotropic material, the shear modulus is related to Young's modulus Y and the Poisson ratio ν by

$$G = \mu = Y/[2(1+\nu)]. \tag{10}$$

The general procedure used in this work was to first calculate the far field part of either the stress field or the strain field as a sum of contributions generated by all the defects. This linear superposition of the stress/strain fields is justified by the linearity of the relationship between stress and strain in the far field region. In general, expressions for either the stress field or the strain field (but not always both) generated by a single defect can easily be found in the scientific literature.[43,44] The equation $\boldsymbol{\sigma}''=\mathbf{C}''\cdot\boldsymbol{\varepsilon}''$ [from Eq. (7)] or the equivalent equation $\boldsymbol{\varepsilon}''=\mathbf{C}''^{-1}\cdot\boldsymbol{\sigma}''$ was used to calculate the complementary field and the strain energy field was then calculated using Eq. (7). The strain energy density in the core regions was then calculated using a constant cutoff $\rho_E^{\max}$ or a cutoff function, which was applied to the contributions of individual defects to the stress or strain field.

Point defects

The displacement caused by a point defect in an infinite linear isotropic body is spherically symmetric and has the form[43]

$$u_r = \frac{\delta v}{4\pi r^2}\frac{\mathbf{r}}{|r|}, \tag{11}$$

where δv is the expansion or contraction (negative δv) induced by the point defect and u_r is the outward pointing displacement vector at a distance $r=|\mathbf{r}|$ from the point defect. The corresponding strain is given by

$$\varepsilon_{rr} = \frac{\delta v}{\pi r^3}$$

and

$$\varepsilon_{\theta\theta} = \frac{\delta v}{2\pi r^3}, \tag{12}$$

where ε_{rr} is the radial and $\varepsilon_{\theta\theta}$ is the tangential strain. While this form for the strain field has manifest spherical symmetry,

Author complimentary copy. Redistribution subject to AIP license or copyright, see http://jcp.aip.org/jcp/copyright.jsp

the local point centered spherically symmetric coordinate system is not convenient for systems with multiple defects.

In Cartesian coordinates, the components of the displacement vector (u_x, u_y, u_z) are given by

$$u_x = \frac{\delta v x}{4\pi(x^2+y^2+z^2)^{3/2}}, \quad u_y = \frac{\delta v y}{4\pi(x^2+y^2+z^2)^{3/2}},$$

and

$$u_z = \frac{\delta v z}{4\pi(x^2+y^2+z^2)^{3/2}} \tag{13}$$

so that

$$\varepsilon_{xx} = \frac{\delta v(y^2+z^2-2x^2)}{4\pi(x^2+y^2+z^2)^{5/2}},$$
$$\varepsilon_{xy} = \varepsilon_{yx} = \frac{-\delta v(3xy)}{4\pi(x^2+y^2+z^2)^{5/2}}, \tag{14}$$

and similar expressions can be obtained for the other components of the strain tensor. Equations (13) and (14) define the strain due to a single point defect located at the origin of a Cartesian coordinate system. They can easily be generalized for a point defect at any position, and the principle of linear superposition can be used to calculate the far field component of the strain tensor for two or more point defects. This equation indicates that the stress and strain fields associated with a single defect scale as $\sigma \sim r^{-3}$ and $\varepsilon \sim r^{-3}$. Consequently, the strain energy density decreases as $\rho_E \sim r^{-6}$. This implies that point defects have only a local effect and that they can lead to the formation of only shallow pits, which soon disappear as the dissolution process continues to lower the surface. Once the strain field has been calculated, the stress field can be calculated using $\boldsymbol{\sigma}'' = \mathbf{C}'' \cdot \boldsymbol{\varepsilon}''$ [from Eq. (7)], and the strain energy density can then be obtained from Eq. (5).

Line defects

In terms of the stress/strain field, the most simple of the line defects is the screw dislocation, which induces purely shear deformation given by[42,44]

$$\varepsilon_{xz}(x,y) = \varepsilon_{zx}(x,y) = -\frac{b}{4\pi}\frac{x}{x^2+y^2}$$

and

$$\varepsilon_{yz} = \varepsilon_{zy} = \frac{b}{4\pi}\frac{y}{x^2+y^2} \tag{15}$$

for an infinite dislocation oriented in the z direction (perpendicular to the dissolving surface). Here, b is the magnitude of the Burgers vector, which defines the strength and direction of the dislocation ($b = \pm|\mathbf{b}|$, where $\mathbf{b}$ is the Burgers vector and the sign of b depends on the sense of the screw). In this equation, x and y are the coordinates in a Cartesian coordinate system with the origin on the center of the line defect and z axis parallel to the direction of the dislocation (the z axis coincides with the axis of the dislocation). All the other components of the strain tensor are zero, and the nonzero components of the stress tensor are given by

$$\sigma_{xz} = \sigma_{zx} = -\frac{\mu b}{4\pi}\frac{x}{x^2+y^2}$$

and

$$\sigma_{yz} = \sigma_{zy} = \frac{\mu b}{4\pi}\frac{y}{x^2+y^2} \tag{16}$$

or

$$\gamma_{xz} = \gamma_{zx} = -\frac{\mu b}{2\pi}\frac{x}{x^2+y^2}$$

and

$$\gamma_{yz} = \gamma_{zy} = \frac{\mu b}{2\pi}\frac{y}{x^2+y^2}. \tag{17}$$

The stress/strain field for an edge dislocation is more complex—it contains both shear and extension/compression components in a coordinate system in which the z component is parallel to the axis of the dislocation. The strain field for an edge dislocation in which the "extra plane of atoms" lies in the xz plane, with $x > 0$, is given by[43,44]

$$\sigma_{xx} = \frac{-\mu b}{2\pi(1-v)}\frac{y(3x^2+y^2)}{(x^2+y^2)^2},$$
$$\sigma_{yy} = \frac{\mu b}{2\pi(1-v)}\frac{y(x^2-y^2)}{(x^2+y^2)^2}, \quad \text{and} \quad \sigma_{zz} = v(\sigma_{xx}+\sigma_{yy}) \tag{18}$$

for the diagonal elements and

$$\sigma_{xy} = \sigma_{yx} = \frac{\mu b}{2\pi(1-\nu)}\frac{x(x^2-y^2)}{(x^2+y^2)^2} \quad \text{or}$$
$$\gamma_{xy} = \gamma_{yx} = \frac{\mu b}{\pi(1-\nu)}\frac{x(x^2-y^2)}{(x^2+y^2)^2} \quad \text{and} \quad \sigma_{xz} = \sigma_{yz} = 0 \tag{19}$$

for the shear components. These equations can also be easily generalized for defects with different positions and Burgers vectors. The strain tensor can be obtained from the stress tensor from $\boldsymbol{\varepsilon}'' = \mathbf{C}''^{-1} \cdot \boldsymbol{\sigma}''$, where the compliance matrix $\mathbf{C}''^{-1}$ has the form

$$\mathbf{C}''^{-1} = \begin{bmatrix} \mathbf{A}^{-1} & \mathbf{0} \\ \mathbf{0} & \mathbf{B}^{-1} \end{bmatrix}. \tag{20}$$

The matrix $\mathbf{A}^{-1}$ is given by

$$\mathbf{A}^{-1} = \frac{1}{Y}\begin{bmatrix} 1 & -\nu & -\nu \\ -\nu & 1 & -\nu \\ -\nu & -\nu & 1 \end{bmatrix} = \frac{1}{2\mu(2\mu+3\lambda)}\begin{bmatrix} 2\lambda+2\mu & -\lambda & -\lambda \\ -\lambda & 2\lambda+2\mu & -\lambda \\ -\lambda & -\lambda & 2l+2\mu \end{bmatrix} \tag{21}$$

and $\mathbf{B}^{-1}$ is a diagonal matrix with diagonal elements equal to $2(1+\nu)/Y = 1/\mu$.

Author complimentary copy. Redistribution subject to AIP license or copyright, see http://jcp.aip.org/jcp/copyright.jsp

KINETIC MONTE CARLO SIMULATIONS

In kinetic Monte Carlo simulations the rates of elementary processes are replaced by probabilities. This method can be applied to a wide variety of processes including chemical reactions,[45] the kinetics of colloidal aggregation,[46] phase separation,[47,48] adsorption and desorption processes,[47] diffusive transport,[49,50] heterogeneous catalysis,[51] and the growth and dissolution of minerals and other materials.[52,53] When kinetic Monte Carlo simulations are used to simulate microscopic processes, the random selection of discrete events introduces "noise" that plays an essential role in the simulation and realistically represents the effects of thermally driven fluctuations.

Here, a kinetic Monte Carlo model is used to simulate dissolution of a solid body represented by "solid" sites in a cubic lattice. In a typical Monte Carlo simulation of dissolution of a solid body with an initially smooth horizontal surface (a surface lying in the xy plane) exposed to a reactive fluid, all of the sites in a cubic lattice with z coordinates of z_0 or smaller are labeled at the start of a simulation to represent the solid material, and the sites at a height greater than z_0 are given a different label to represent a fluid phase. In a solid-on-solid models, like those used in this work, dissolution is represented by removal of only the highest "occupied" (labeled as solid) sites in each column of occupied sites. This allows the cubic lattice to be dispensed with, since the model system is completely defined by the highest occupied, solid filled, site in each column of the lattice, and the system can be represented by the height field $h(x,y)$—the height of the surface of the solid at lateral position (x,y), where (x,y) is a discrete coordinate system ($x=n_x a$ and $y=n_y a$, where n_x and n_y are integers and a is the length of the side of a unit cell of the cubic lattice). Each time the height of a column is reduced by unity, to represent a dissolution event, the coordination number of the site at the top of that column and the coordination numbers for the sites at the tops of the four nearest-neighbor columns may change. Consequently it is necessary to determine if the coordination numbers in these sites have changed and, if necessary, update the corresponding reaction rates after every dissolution event is executed. The coordination numbers n for the site at lateral position (x,y) can be calculated directly from the height of surface at (x,y) and the heights at lateral positions $(x+1,y)$, $(x-1,y)$, $(x,y+1)$, and $(x,y-1)$ using the expression

$$n = 1 + m(h(x+1,y) - h(x,y)) + m(h(x-1,y) - h(x,y)) + m(h(x,y+1) - h(x,y)) + m(h(x,y-1) - h(x,y)), \tag{22}$$

where $m(\delta h)=1$ if $\delta h \geqslant 0$ and $m(\delta h)=0$ if $\delta h < 0$.

Periodic boundary conditions were used in the lateral directions (parallel to the initial surface) in all of the simulation of dissolution processes. Consequently, the system can be thought of as an infinite array of identical domains of size $L_x \times L_y$, which compactly tile two-dimensional space. This means that cells at the edge of the computational domain are treated in exactly the same way as cells in the interior of the computational domain, even though neighboring cells might lie in a periodic image of the computational domain. In other words all coordinates are treated using modular arithmetic with a modulus of L_x in the x direction and a modulus of L_y in the y direction.

To calculate the stress/strain fields, full periodic boundary conditions were not used. In simulations in which a single line defect was located in the center of the computational domain, only the contribution of this single defect to the stress/strain fields was calculated (the effects of image defects in adjacent domains were ignored). For simulations with multiple defects, some account of overlapping stress/strain fields from image cells was required. In molecular dynamics[54–57] and Monte Carlo[58–61] simulations of ionic and dipolar materials, Ewald summation over all the periodic images[62] has been used extensively to calculate long-range electrostatic interactions. There is a strong analogy between electric fields generated by charges and stress/strain fields generated by defects (the defects act as sources for stress and strain in much the same way that charges act as sources for electric fields) and Ewald summation or other rapidly convergent methods such as multipole expansions and lattice summation could be used to calculate the stress/strain fields in periodic systems containing many defects. However, the simple approach of including only the contributions from the defects in the central domain of size $L_x \times L_y$ and the eight neighboring domains in the 3×3 array of domains of size $L_x \times L_y$ nearest to the central domain (the nearest-neighbor and next-nearest-neighbor domains) was adopted. In all of the simulations with multiple screw defects, the numbers of defects with Burgers vectors $\mathbf{b}$ of $+bz$ and $-bz$ were equal. This is equivalent to keeping the number of positive and negative charges equal to ensure overall charge neutrality. The large number of screw defects in a domain and the large scale of the domains both contribute to the relatively small errors (relative to the stress/strain fields in an equivalent infinitely periodic system). For example, for simulations presented below involving 100 screw dislocations randomly inserted in an area of $L_x \times L_y = 2024 \times 2024$, the contribution to the xz component of the strain field due to the defects in the 16 domains $(5\times 5 - 3\times 3)$ bordering the central 3×3 block ranged between -1.7×10^{-5} and 1.5×10^{-5}, and the contribution to the yz component of the strain field ranged between -1.6×10^{-5} and 3.2×10^{-5}. Similarly, the contribution from the next shell of 24 $(7\times 7 - 5\times 5)$ domains surrounding the central 5×5 block of domains to the xz component of the strain field in the central domain ranged between -3.4×10^{-6} and 3.1×10^{-6}, and the contribution to the yz component of the strain field in the central domain ranged between -3.4×10^{-6} and 6.1×10^{-6}. This indicates that a simple shell by shell summation is quite rapidly convergent and that neglect of the domains outside of the central 3×3 block leads to an error of less than 5×10^{-5} in the strain field. This means that the relative error near to the line defects, where the effects of the stress/strain fields are the most important, is less than 10^{-3}. To put this into a physical context, for a material with a compression modulus of 100 GPa, a strain of 5×10^{-5} would correspond to a pressure of 5 MPa which is the hydrostatic pressure at a depth of 500 m. At a distance of r_c, the cutoff distance, the magnitude of the strain is $O(10^{-1})$.

A similar procedure was used for the simulations of dis-

Author complimentary copy. Redistribution subject to AIP license or copyright, see http://jcp.aip.org/jcp/copyright.jsp

solution controlled by multiple edge dislocations. In this case, equal numbers of edge dislocations with Burgers vectors (x,y) of (1,0), (−1,0), (0,1) and (0,−1) were used.

During each step in the simulation a column in the lattice [a lateral position (x,y)] is selected randomly and the height at that position is reduced by unity (in lattice units) with a probability

$$P_i \propto R_i, \tag{23}$$

where the dissolution rate R_i is given by Eq. (4).

Two simple kinetic Monte Carlo algorithms can be used to simulate dissolution based on these ideas. The first algorithm is closely related to the standard Monte Carlo algorithm for equilibrium systems,[63] and it will be referred to as the "random select and test" algorithm. In this algorithm, a column of the lattice is selected randomly and the height of that selected column is reduced by unity with a probability $P_{s,i}$ given by $P_{s,i}=R_i/R_{\max}$, where $R_{\max}$ is the maximum dissolution rate for any surface site at the top of a column. This is implemented by selecting a random number x from a uniform distribution over the range $(0<x<1)$ and executing the randomly selected event if and only if $x<P_{s,i}=R_i/R_{\max}$. If this approach is used, then the kinetics of dissolution can be simulated by incrementing the time by an amount δt_1 given by $\delta t_1=1/N_S R_{\max}$, where N_S is the number of columns in the lattice (the number of active surface sites, $L_x\times L_y$) every time a column is selected and an "attempt" is made to reduce the height of that column. If the range of reaction rates is small, this method can be computationally efficient, but for many problems its performance is very poor. For a domain size of $L_x\times L_y$, the computer time t_{comp} required to reduce the average height of the surface by a (or unity since a is the unit of length) scales as $t_{\text{comp}}\sim L_x\times L_y\times R_r$, where R_r is the ratio between the fastest and the average rate ($R_r=R_{\max}/\langle R_i\rangle$). This is the inverse of the acceptance ratio (the fraction of attempted events that are accepted and result in removal of a site from the surface). For the cubic lattice model, in the absence of the effects of strain, the ratio R_r is given approximately by $R_r=e^{(2E_b)}$, and for a mineral such as quartz[26] with $E_b\approx 10$, $R_r\approx 5\times 10^8$. Even for a mineral with a low dissolution activation energy of $E_b\approx 4$, $R_r\approx 3000$. If the effects of the elastic strain are included, the acceptance ratio will typically be less than 10^{-4}, even for a small bond-breaking activation energy ($E_b\approx 4$), which makes the model disastrously slow for this and many other applications.

In the second implementation, which will be referred to as the "running sum algorithm" a running sum R_s of all of the dissolution rates is calculated and the site for which $R_s(i-1)<xR_s(N_S)\leqslant R_s(i)$ is removed to represent dissolution, where x is a number selected randomly from a uniform distribution over the range of $0<x<1$ and $R_s(N_S)$ is the end member of the running sum (the sum of all the dissolution rates). If this approach is used, then the kinetics of dissolution can be simulated by incrementing the time by an amount δt_2 given by $\delta t_2=1/R_s(N_S)$ every time a dissolution event is selected. Although the acceptance ratio is unity for the second method, this method is also slow because $L_x\times L_y$ floating point operations are needed to reconstruct the running sum after each step in the simulation, and an average of $0.5L_x\times L_y$ floating point tests are needed to determine which site should be removed. This means that the computer time required for a simulation scales as $t_{\text{comp}}\sim(L_x\times L_y)^2$. For a large-scale simulation ($L_x\approx L_y\approx 1000$) this approach is impractical. For a lattice with $L_x\times L_y=1024\times 1024$ active surface sites, approximately 6 h of CPU time is required to lower the average surface height by one lattice unit (remove 10^6 sites from the lattice) with this algorithm using a single 2.4 GHz Pentium® 4 processor on a Dell workstation.

These primitive methods were used during the early stages of the investigation, but it soon became evident that it would not be possible to carry out simulations with the large lattices required for many dislocations using these approaches. One important step was to develop a simple method for randomly selecting a dissolution event in a time of order $\log_2(L_x\times L_y)$. This can be accomplished by first determining if $xR_s(N_s)$ is larger or smaller than $R_s(N_0)$, where N_0 is the smallest power of 2 larger than $N_s/2$. If $xR_s(N_s)$ is smaller than $R_s(N_0)$ then $xR_s(N_s)$ is compared with $R_s(N_0-(N_0/2))$ and if $xR_s(N_s)$ is larger than $R_s(N_0)$ then $xR_s(N_s)$ is compared with $R_s(N_0+(N_0/2))$. If in the next stage, for example, it is found that $xR_s(N_s)$ is smaller than $R_s(N_0+(N_0/2))$ [and larger than $R_s(N_0)$], then $xR_s(N_s)$ is compared with $R_s(N_0+(N_0/2)-(N_0/4))$. The process is repeated until the nth stage at which $N_0/2^n=1$. This locates the interval in the running sum that contains $xR_s(N_s)$ within ± 1, and the interval which contains $xR_s(N_s)$ can then be determined by comparison with the values of adjacent elements in the running sum. (The location of the required event in the running sum is either $N_x=N_0\pm N_0/2\pm N_0/4\cdots\pm 1$ or N_x+1). Theoretically, this accelerates the selection process by a factor of approximately $L_x\times L_y/\log_2(L_x\times L_y)\approx 5\times 10^4$ for $L_x=L_y=1024$. However, the problem of recalculating the running sum remains. This can be addressed by continuing the running sum as new surface sites are created or the reaction rates of surface sites change. A linear logical or integer array whose elements have a 1:1 correspondence with the elements of the running sum is used to distinguish "dead" events (events that are no longer possible because of the evolution of the interface) from "live" events. After an event has been selected, it is executed only if that event is still "alive." A new running sum containing $L_x\times L_y$ elements is constructed if the length of the running sum reaches $N_{\text{ex}}\times L_x\times L_y$ elements, where N_{ex} is a small number greater than unity, or if the maximum of the running sum (the value of its end member) exceeds M_{ex} times the sum of the rates of the still active processes, where M_{ex} is another small number greater than unity. The numbers N_{ex} and M_{ex} should be kept small to keep the acceptance probability high and to control memory requirements, but larger values reduce the frequency with which a completely new running sum must be recalculated. Unfortunately, this approach improved the speed of the simulations by a factor of only about 2. The reason for this poor performance is that the rates of most dissolution events that actually take place are much larger than the average dissolution rate. Consequently, the large elements in the running sum die quickly, and the acceptance ratio also declines quickly as the probability of selecting a dead event increases. This problem can be substantially alleviated by using two

Author complimentary copy. Redistribution subject to AIP license or copyright, see http://jcp.aip.org/jcp/copyright.jsp

running sums—one for the fast events and one or the slow events. The short running sum for the fast events is refreshed frequently and the long running sum for the less frequent events is refreshed less frequently. This algorithm will be referred to as the "extended running sum" algorithm. In the absence of defects, the dominant dissolution event is the removal of a three coordinate kink site at a terrace edge if the bond-breaking activation energy is more than a few times k_BT. From Eq. (2), the rate of this event is $R_{\text{typical}}=Ae^{-(3E_b)}$. In simulations of the formation of shallow etch pits in which dissolution events larger than $0.5R_{\text{typical}}$ were considered to be fast events, the times required to reduce the height of the surface by one lattice unit from a system with $L_x \times L_y = 1024 \times 1024$ were about 12 s for a bond-breaking activation energy of $E_b=10$ and about 10 s for $E_b=5$. In these simulations N_{ex} and M_{ex} were both assigned values of 2. No systematic attempt was made to vary the values of N_{ex} and M_{ex} or the threshold between fast and slow events, and it is possible that the performance of this algorithm could be improved by a better selection of these parameters. On the other hand, the optimal values for these quantities will vary with model parameters, and our objective was to develop algorithms fast enough to achieve our research objectives rather than to achieve the best possible performance in each simulation. To implement this algorithm, it is necessary to keep track separately of the possible fast and slow events as the dissolving surface evolves. For typical parameters (E_b and the parameters associated with the strain energy density), this is about 2000 times faster than the best of the primitive algorithms (the running sum algorithm) described above for systems of size $L_x \times L_y = 1024 \times 1024$.

Another approach, which will be referred to as the "divide and conquer" algorithm, was developed after the simulations with point defects were completed. This algorithm is based on the idea of classifying dissolution events according to their rates and treating the events in each class separately using the random select and test approach. This method is efficient because the range of rates in every class is small. The rates are divided into N_b equal intervals (rate classes) on a logarithmic scale ranging from the minimum rate to the maximum rate. An event is selected randomly by first randomly selecting one of the classes, with probabilities proportional to $N_cR_c^M$, where N_c is the number of members in a class and R_c^M is the maximum rate for members of the selected class. Once the class has been selected a member of the class is selected randomly and the selected member is accepted if a random number x uniformly distributed over the range $0<x<1$ is smaller than R/R_c^M, where R is the rate of the selected class member (the selected process). The probability that a particular even with a rate R will be selected is given by the product of the class selection probability ($N_cR_c^M/\Sigma_{c'}N_{c'}R_{c'}^M$), the probability that the event will be accepted within its class ($1/N_C$), and the acceptance probability (R/R_c^M). This indicates that the event selection probability is

$$R/R_c^M \times 1/N_C \times N_cR_c^M \Big/ \sum_{c'} N_{c'}R_{c'}^M = R \Big/ \sum_{c'} N_{c'}R_{c'}^M \tag{24}$$

and that the time should be incremented by $1/\Sigma_{c'}N_{c'}R_{c'}^M$ every time an attempt is made to execute an event. It is essential that the probability of selecting an event is proportional to its rate, and Eq. (24) shows that this condition is satisfied. To maintain a high acceptance rate the ratio R_c^M/R_c^m must be kept small, where R_c^m is the minimum rate in the class (R_c^M/R_c^m has the same value for all classes). Suitable values for R_c^M/R_c^m lie in the range of 2.0–4.0. For $E_b=10.0$ and a maximum strain energy of 7.5, this implies that the number of classes should lie in the range of $50/\ln(4) \leqslant N_c \leqslant (50)/\ln(2)$ or $18 \leqslant N_c \leqslant 36$. This is an exceptionally large range of rates (a ratio of almost 10^{22} between the fastest and slowest rates). For more typical parameters, the range of rates is smaller, and about 20 classes is sufficient (this would allow a ratio greater than 10^{12} between the fastest and slowest rates for $R_c^M/R_c^m=4$). It is desirable to keep N_c small because a new running sum of the class selection probabilities $N_cR_c^M$ must be calculated during each step in the simulation. In practice, the speed of the simulation is not very sensitive to N_c because other parts of the simulation (primarily calculating the rates for the new events that are possible when the surface changes, determining which class the new events belong to and book keeping), require more time. An important advantage of the divide and conquer method over the extended running sum method is that only one quantity (N_c) affecting the performance must be selected while three quantities ($N_{\text{ex}}, M_{\text{ex}}$, and the threshold between the fast and slow events) must be selected if the extended running sum method is used. Also, the performance of the divide and conquer method is not very sensitive to N_c. The overall performance of the divide and conquer algorithm is somewhat better that that of the extended running sum method, and the time required to reduce the height of the surface by one lattice unit for a system with $L_x \times L_y = 1024 \times 1024$ was 4.0–4.5 s. The speedups relative to the most simple running sum method for different system sizes were 3.5 (32×32), 11 (64×64), 44 (128×128), 185 (256×256), 880 (512×512), 4175 (1024×1024), $>15\,000$ (estimate) (2048×2048), $>50\,000$ (estimate) (4096×4096) for a test case with ten screw dislocations and a bond-breaking activation energy of 4.0. Further improvements might be possible, but more complex schemes require more book keeping overhead. Substantial improvements in one part of the code do not necessarily lead to substantial improvements in overall performance. The simple strategy of keeping track of which class of events is executed more frequently and then determining whether or not this class would be selected before executing a fast comparison between a random number and the running sum of class selection probabilities *increased* cpu time, despite the fact that in typical simulations most events do belong to only one class.

The divide and conquer approach is particularly efficient when there is a small number of discrete rates. In this event, the rate classes have a 1:1 correspondence with the discrete rates and the acceptance ratio is unity for each rate class. In

Author complimentary copy. Redistribution subject to AIP license or copyright, see http://jcp.aip.org/jcp/copyright.jsp

addition, if the number of distinct rates is small, then the running sum is short and both the reconstruction of the running sum and the random selection of a rate class (weighted by the sum of the rates of the events in each class) are correspondingly fast. However, simulations carried out using the divide and conquer algorithm are only about two times slower than simulations carried out using the simplified model in which the effects of the stress/strain field is ignored and there is only a small number (five for a cubic lattice) of discrete rates. This model has an acceptance ratio of unity, and there is no need to construct a running sum. The speed of the simplified model provides an upper limit for the speed of simulations carried out using the divide and conquer model. This indicates that the potential for further improvements in the divide and conquer algorithm is relatively small. A significant disadvantage of the divide and conquer algorithm is the amount of memory that it requires. In its present form this limits effective use of the algorithm to surfaces of about (2048×2048) or smaller for a typical single processor workstation. The memory requirements could be reduced, but only at the cost of increased book keeping overhead. The extended running sum method used less memory, and we have performed simulations on systems of size (4096×4096) using this method.

Maksym[64] developed a kinetic Monte Carlo model for molecular beam epitaxy, which is based on dividing the $N_{\text{tot}}=L_x\times L_y$ events into N_g groups, each containing $g=N_{\text{tot}}/N_g$ events. The algorithm consists of first selecting a group and then selecting a specific event within the chosen group. The optimum value of N_g is approximately $N_{\text{tot}}^{1/2}$ and this leads to an acceleration by a factor of $O(N_{\text{tot}}^{1/2})$. We were unaware of the work of Maksym when the methods described above were developed, and we have not implemented this method to evaluate its efficiency. However, the accelerations obtained from the divide and conquer and extended running sum methods described above are greater than $N_{\text{tot}}^{1/2}$, and they are almost certainly more efficient than Maksym's method.

Point defects

If a material is subjected to elongational deformation, the strain energy is given by

$$E_\varepsilon = \varepsilon^2 YV/2, \tag{25}$$

where ε is the elongational strain, E_ε is the strain energy in Newton meters (or Joules), Y is Young's modulus in pascals, and V is the volume of strained material in cubic meters. In the Monte Carlo simulations k_BT is the unit of energy and the length a of the unit cell in the cubic lattice is the unit of length. The strain energy is given by

$$E_{\varepsilon m} = \varepsilon^2 Y_m V_m/2, \tag{26}$$

where $E_{\varepsilon m}$ is the strain energy in units of k_BT, Y_m is Young's modulus in computer model units [defined by Eq. (25)], V_m is the volume of the strained material in units of a^3, and a is the length of a lattice unit (the distance between the centers of two nearest neighbor cells in the lattice). To make the energies in Eqs. (25) and (26), measured using the same

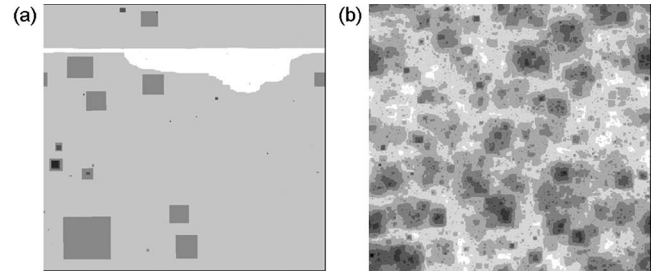

FIG. 1. Results of a simulation of dissolution with a point defect density of 6×10^{-6}. On the left-hand side (a), the bond-breaking activation energy is 10, while on the right-hand side (b), the bond-breaking activation energy is 4. The gray scale indicates the height of the surface (a darker shade indicates a lower height), which is shown after an average of 20 layers have been removed. A similar gray scale is used to indicate the surface height in all of the simulations. The surface area is $L_x\times L_y=1024\times 1024$.

units, equal for equal volumes of material subjected to the same strain, $E_{\varepsilon m}$ and E_ε must be related by

$$E_{\varepsilon m} = E_\varepsilon/1.380\,65\times 10^{-23}, \tag{27}$$

where $1.380\,65\times 10^{-23}$ is the Boltzmann constant in units of J K^{-1}. This implies that

$$Y_m V_m = YV/1.380\,65\times 10^{-23}, \tag{28}$$

and Young's modulus Y_m used in the computer model must be related to Young's modulus in pascals Y_{Pa} by

$$Y_m = \frac{Y_{\text{Pa}}\times\delta^3}{1.380\,65\times 10^{-23}\times T} = \frac{Y_{\text{Pa}}\times v}{1.380\,65\times 10^{7}\times T} = \frac{Y_{\text{GPa}}\times v}{3.865}, \tag{29}$$

where δ is the length in meters corresponding to one side of a unit cell, v is the volume represented by a unit cell in the cubic lattice in units of Å^3, and Y_{GPa} is Young's modulus in gigapascals. A temperature of 280 K has been assumed in the expression on the right hand side. Furthermore, if Young's modulus of 87 GPa and a unit volume of 37.6 Å^3 (the average Young's modulus and the volume of a SiO_2 unit in quartz) are assumed, then the above equation indicates that a value of about 850 should be used for Young's modulus Y_m in the kinetic Monte Carlo model. This value for Y_m and a Poisson ratio of $\nu=0.3$ were used in almost all of the simulations presented here. In real inorganic crystals, Young's modulus covers a quite wide of values; it has a value of about 5.3 GPa for cesium iodide and almost 1200 GPa for diamond.

If the magnitude of the expansion $|\delta v|$ (the strength of the point dislocation) is assumed to be $0.5v$, and it is assumed that the theory of linear elasticity can be applied only for strains smaller than 0.1, then Eq. (11) implies that the radius of the disordered core region is only slightly larger than a. Figure 1(a) shows results from a simulation carried out using the parameters $Y_m=850$, $\delta v=0.5$, $E_b=10.0$, a core radius of $r_c=1.2$ (in units of a), and a Poisson ratio of $\nu=0.3$. Figure 1(b) is for the same conditions except with $E_b=4.0$. The point defects were inserted randomly with a minimum separation of 10 lattice units. With these parameters, the maximum strain energy, in the core, is about 10 (in units

Author complimentary copy. Redistribution subject to AIP license or copyright, see http://jcp.aip.org/jcp/copyright.jsp

of k_BT). This implies that once the core is exposed, the core sites will dissolve $e^{10} \approx 2 \times 10^4$ times faster than sites in an unstrained part of the surface. A defect density of 6×10^{-6} (in units of a^{-2}, where a is the length of a cell in the simulation lattice) was used to obtain the results in Fig. 1. At this low defect density, more pits are initiated spontaneously than by exposure of point defects. However, the spontaneously initiated pits have a depth of only one lattice unit, while the pits initiated by exposed point defects are several lattice units deep.

In the simulations shown in Fig. 1, the strain energy density $\rho E(x)$ was calculated at the centers of all of the cells in a three-dimensional lattice, and the regions occupied by solid and fluid were represented by "labeling" a three-dimensional lattice. Because of the short range of the stress/strain field associated with each defect and the restriction on the distance between neighboring defects, the strain energy density $\rho_E(r)$, where r is the distance from the defect, can be calculated for each defect and the contribution of each defect can be added [$\rho_E^T(x) = \Sigma_{i=1}^{i=N_d} \rho_E(|x - x_i|)$, where i is the position of the ith point defect, $\rho_E^T(x)$ is the total strain energy density at position x, and N_d is the total number of point defects]. These procedures are very much different from those used for line defects, and they cannot be used for line defects. To account for the behavior in the core region, the relationship between strain energy density and the distance from the center of the defect was changed from $\rho_E \sim r^{-6}$ to $\rho_E \sim (r^2 + r_c^2)^{-3}$ or $\rho_E \sim r^{-6} f_c(r)$, where $f_C(r) = r^6/(r_c^2 + r^2)^3$. The cutoff function $f_C(r)$ has the forms $f_C(r) \to 1$ for $r \gg r_c$ and $f_C(r) \to r^6/r_c^6$ for $r \ll r_c$. This removes the singularity in the strain energy density calculated using the theory of linear elasticity. Without guidance from more detailed simulations, the form of the cutoff function is arbitrary, providing it satisfies $f_C(r) \to 1$ for $r \gg r_c$ and $f_C(r) \to r^6/\text{Const.}$ for $r \ll r_c$. Because of the short range of the stress/strain field surrounding a point defect, the primary effect of the point defects on the dissolution process is to initiate shallow pits. This observation motivated the development of a simplified "no strain/empty core" model in which the effect of the point defects is represented by removing a small cluster of sites from the surface when a point defect is encountered and the effects of the strain associated with the point defects are ignored. Figure 2 shows the results of simulations carried out using this model. A pit nucleus consisting of 15 sites [a pattern consisting of a site and its four nearest neighbors in the (x,y) plane repeated at three adjacent heights] representing the highly deformed core of a point defect, together with any occupied sites above the pit nucleus, was removed whenever the core of a point defect was uncovered. Figure 2(a) shows a simulation carried out using this simplified model with a bond-breaking activation energy of 10, and Fig. 2(b) shows a simulation carried out with a bond-breaking activation energy of 4. Since the strain energy is neglected in this model, there are only five distinguishable dissolution rates, corresponding to one to five bonds connecting any particular surface site to the bulk solid. This makes it possible to develop a very efficient model at the cost of some book keeping and overhead by keeping track separately of the surface sites with different coordination numbers. In each step of the simulation the coordination number n of the site to be removed is first selected, based on the product of the number of sites of each coordination number and their dissolution rates (the total dissolution rate for solid sites with coordination number n), and then a specific site with that coordination number is randomly selected and removed. Using this model, $L_x \times L_y = 1024 \times 1024$ sites can be removed in $O(1)$ s.

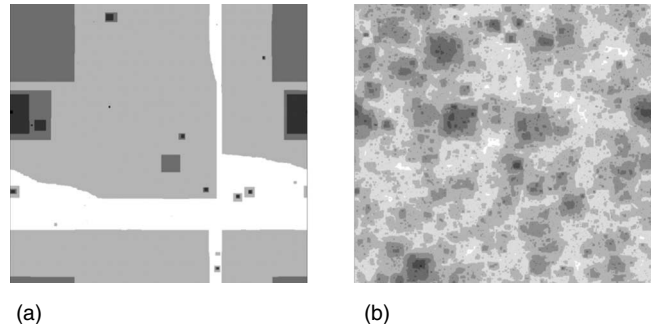

FIG. 2. Results from a simulation carried out using the simplified no strain/empty core model for dissolution of a solid containing point defects. The point defect density is 6×10^{-6}. On the left-hand side (a), the bond-breaking activation energy is 10, while on the right-hand side (b), the bond-breaking activation energy is 4. The volume of the defect core, which dissolves instantaneously on exposure, was 15 (in units of $v = a^3$). The gray scale indicated the height of the surface, which is shown after an average of 20 layers have been removed. The surface area is $L_x \times L_y = 1024 \times 1024$.

A comparison of Figs. 1 and 2 show that the simplified no strain/empty core model gives results that are very similar to those obtained from the more complete model. For each model, there are substantial differences between different realizations obtained by using a different set of random numbers. It could be argued that the simplified model cannot be used to address issues such as the dependence of the pit depth on the defect strength δv. On the other hand, the effects of point defects are dominated by the poorly understood core region, and, in most cases, it is not possible to reliably estimate the cutoff radius or the form of the cutoff function. Molecular dynamics simulations could be helpful, but accurate particle-particle or multiparticle interaction potentials are often not available for important minerals.

Simulations were also carried out using models that were based on the idea that the stress/strain fields are relaxed as soon as the dissolving surface reaches the center of the point defect (vacancy, interstitial, or impurity). Although the surface morphology is changed somewhat by this relaxation process, the essential nature of the dissolution process remains the same—point defects initiate shallow pits which grow laterally and merge in combination with pits that are spontaneously initiated. The simplified, no strain/empty core, version of this model is the same as the simplified no strain/empty core model without relaxation, except for a smaller effective core volume. The amplitude of the surface roughness generated in this manner is just a few lattice units (like the surfaces shown in Figs. 1 and 2).

Screw dislocations

Simulations based on Eqs. (8), (9), and (19)–(21) were carried out to investigate the influence of screw dislocations on dissolution. Figure 3 shows how the nature of single pits

Author complimentary copy. Redistribution subject to AIP license or copyright, see http://jcp.aip.org/jcp/copyright.jsp

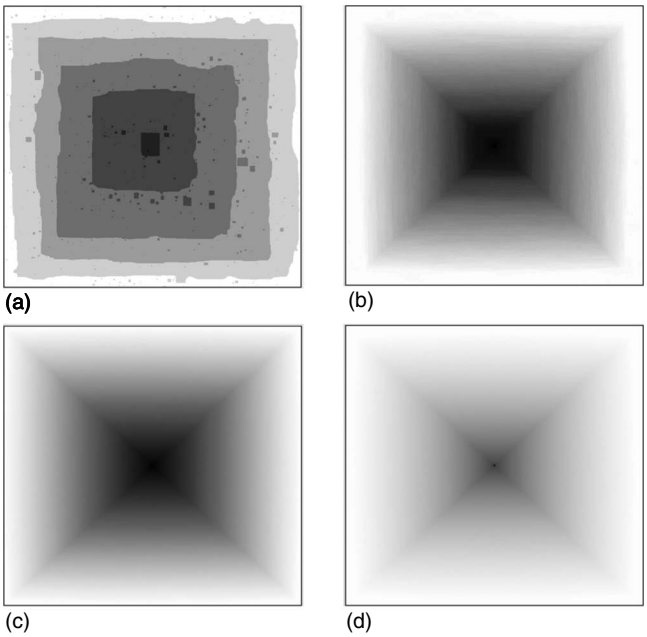

FIG. 3. Isolated pits centered on screw dislocations. The pits were generated with a shear modulus of $G_m=370$, a Burgers vector with a magnitude of unity and bond-breaking activation energies of $E_b=6.5$, 5.0, 3.5, and 3.0 in (a), (b), (c), and (d). The simulations were carried out using lattices of $L_x \times L_y=1024\times 1024$ sites, and the average height was reduced by 50, 50, 500, and 500. The simulations were stopped when the pit growth (approximately) reached the edges of the lattice, and the pit depths (the difference between the maximum and minimum heights shown in the 1024×1024 areas) at this stage were 6, 55, 524, and 1171. The apparently darker gray shade along the diagonal corners in (b)–(d) is an optical illusion, and this can be confirmed by covering three of the four quadrants with white paper.

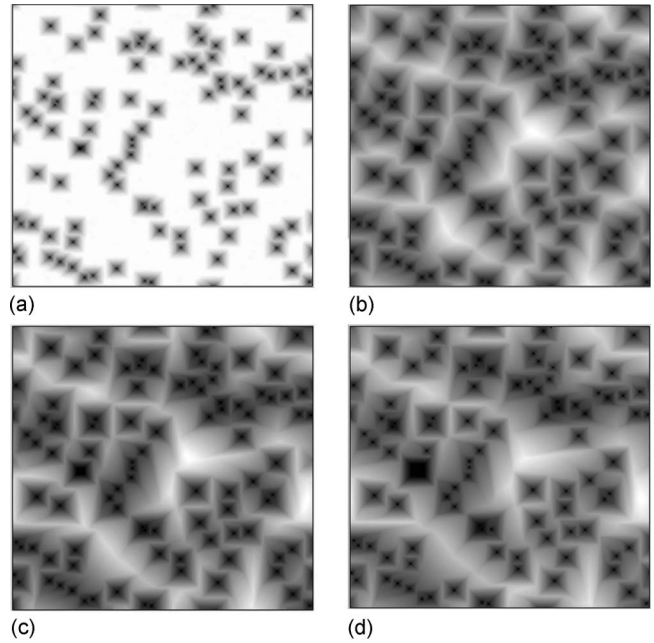

FIG. 4. Four stages in a simulation of dissolution of a 2048×2048 surface with 100 randomly distributed dislocations. This simulation was performed using Young's modulus of $Y=850$, a Poisson ratio of $\nu=0.3$, a Burgers vector with a value of unity, $b=1$, and a bond-breaking activation energy of $E_b=3.0$). A sharp cutoff in the total strain energy density corresponding to a cutoff distance of $r_c=1.5$ for an isolated screw dislocation was used. (a)–(d) show the surface after the average height of the surface has been reduced by 40, 320, 1280, and 5120.

generated with Young's modulus of $Y_m=850$, a Poisson ration of $\nu=0.3$ (a shear modulus of $G_m=327$), a Burgers vector with magnitude $b=1$, and a cutoff length of $r_c=1.2$ depends on the bond-breaking activation energy E_b. In these and other simulations with screw dislocations and edge dislocation, it was assumed that the dislocations are oriented perpendicular to the plane of the dissolving surface. The singularities in the stress/strain fields were removed by replacing $x^2+y^2=r^2$ in the denominator in Eqs. (19)–(21) by $(r^4+r_c^2r^2)^{1/2}$. For an isolated defect this changes the strain energy density from $\rho_E\sim r^{-2}$ to $\rho_E\sim 1/(r_c^2+r^2)$ so that the cutoff function is $f_C=r^2/(r^2+r_c^2)$. Again, the form of this cutoff function is arbitrary, providing that the cutoff function $f_C(r)$ decreases monotonically with decreasing r, with $f_C(r)\rightarrow 1$ for $r\gg r_c$ and $f_C(r)\rightarrow r^6/\text{Const.}$ for $r\ll r_c$. If more than one line defect is present, the effect of the cutoff procedure is more complex.

If the bond-breaking activation energy is large enough, the overall lowering of the surface due to spontaneous nucleation and growth of shallow pits is faster than the recession of the surface due to the strain energy associated with the dislocation, and pits do not develop. Although dissolution is a kinetic process, this behavior is related to the thermodynamics of hollow core formation. The bond-breaking activation energy is related to the surface tension (a large bond-breaking activation energy implies a large surface tension), and the thermodynamic theory of Frank[21] and Cabrera *et al.*[20] predicts that the hollow core radius decreases with increasing surface tension.

For a bond-breaking activation energy of $E_b=6.5$, a relatively shallow pit with sides that have a very small slope [Fig. 3(a)] develops. In this simulation, many small very shallow pits that spontaneously formed within the larger pit nucleated by the screw dislocation can be seen. As the bond-breaking activation energy decreases [Figs. 3(b) and 3(c)] the slope of the pit walls increases. Under these conditions ($E_b=5.0$ and $E_b=3.5$) the influence of the dislocation stress/strain energy is small, except in the immediate vicinity of the dislocation, and the walls of the pits are essentially inclined planes. At sufficiently small bond-breaking activation energy [$E_b=2.0$, Fig. 3(d)], the center of the pit deepens rapidly, and the pit develops a characteristic flared shape near its center. In real crystals, the bond-breaking activation energy will be correlated with the modulus, and it may not be realistic to vary the bond-breaking activation energy over a wide range with a fixed shear modulus. However, the ratio between the bond-breaking activation energy and the shear modulus is not fixed, and the geometry of real etch pits can be expected to depend on the ratio between these parameters. The ratio between the bond-breaking activation energy E_b and the strain energy, Yb^2a^3/r_c^2, where b, a, and r_c are in physical units, or Y_mb^2/r_c^2, where $b,a=1$, and r_c are in model units, is an important dimensionless ratio.

Figure 4 shows some of the results obtained from a simulation in which 100 screw dislocations were placed randomly in a surface with an area of $L_x\times L_y=2048\times 2048$. In a physical system, this would correspond to a dislocation density of $O(10^8)$ cm^{-2}, which is within the range found in real materials (10^6–10^{11} cm^{-2}). The stress and strain fields at

Author complimentary copy. Redistribution subject to AIP license or copyright, see http://jcp.aip.org/jcp/copyright.jsp

every site on the lattice were calculated using the theory of linear elasticity and then reducing any strain energy densities that exceeds $\rho_E^{\max}=G_m b^2/r_c^2 8\pi^2$ to $\rho_E^{\max}$. This is consistent with the idea that the structure in the highly deformed core region is liquidlike[65] and that the largest strain energy density corresponds to this liquidlike structure. Several other models for the cutoff on the strain energy density were investigated. If the stress and strain fields associated with the screw dislocations are calculated with the cutoff function used for the single dislocation simulations illustrated in Fig. 3 and these stress/strain field are summed and then used to calculate the strain energy density, the pits associated with the near coincidence of two or more dislocations completely dominate the pitting pattern on the time scale of the simulations. This occurs because the strain energy density near two, or more, adjacent dislocations exceeds the maximum strain energy density for a more isolated dislocation, and this results in very rapid pit growth. The appealing concept of a liquidlike core suggests that a maximum strain energy density cutoff is more realistic than the additive superposition of the stress and strain fields associated with each of the dislocations, with the same cutoff function for the stress/strain fields associated with each of the dislocations. However, detailed atomistic simulations for specific materials, beyond the scope of this investigation, would be required to resolve this issue.

The main effect of the near coincidence of two or more dislocations is that the pit width deep inside the "coalesced" pit is much greater than the width at a similar level in pits centered on single defects. It is not possible to conclude from the results shown in Fig. 4 what the asymptotic (long time) behavior will be. Although the differences between Figs. 4(c) and 4(d) are small, it is clear that a stationary surface morphology has not been reached, and very much larger scale (larger time) simulations would be required to resolve this issue. However, this is much more of a theoretical issue related to the behavior of the model than a practical issue related to the dissolution of real minerals. An array of infinitely long screw defects, all oriented perpendicular to the plane of the dissolving surface, cannot be generated, and it is certainly not characteristic of real minerals produced under natural conditions. Very often dislocations form loops with characteristic length of $O(1)$ μm and complex structures spanning a wide range of submicron and supramicron length scales,[66–69] and a height reduction, $-\langle\delta h\rangle$, of 5120 in our simulations corresponds to the dissolution of $O(1)$ μm of material from the surface.

To further investigate the factors that control the evolution of the surface morphology, simulations were carried out using a symmetric array of 8×8 dislocations in a surface of 2048×2048 sites. The signs of the Burgers vectors were arranged in a checkerboard fashion (positive on "black" squares and negative on "white" squares), and for each site on the lattice the contributions to the stress/strain fields were calculated from the dislocations lying in a 4096×4096 block, in the periodically continued array of domains, centered on that site. This ensures that each dislocation is in the same environment (stress field and strain field). Figure 5 indicates how the surface evolves under these conditions for

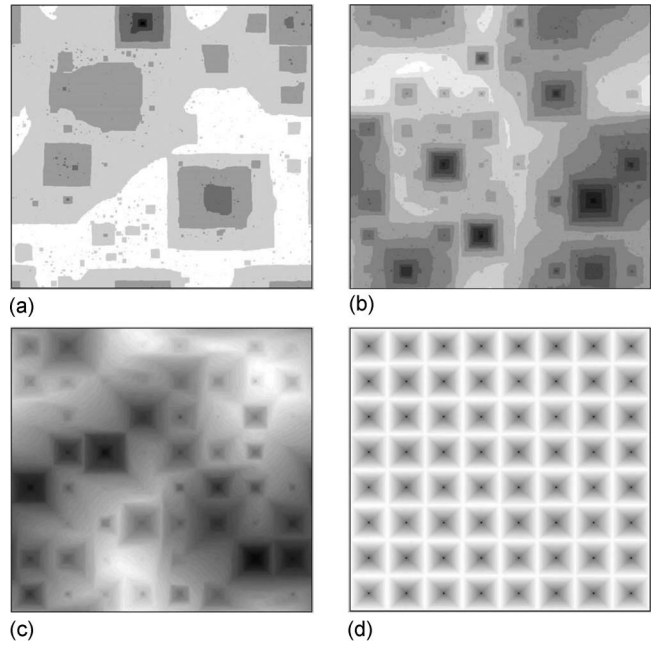

FIG. 5. Pitted surfaces obtained using a symmetric 8×8 array of screw dislocations. The stress/strain fields were calculated using the parameters $Y=850$, $\nu=0.3$, and $b=1$, with a sharp cutoff in the total strain energy density corresponding to a cutoff distance of $r_c=1.5$ for an isolated screw dislocation. (a) shows a simulation with a bond-breaking activation energy of $E_b=7.0$ after the average surface height had been reduced by $\langle\delta h\rangle=320$. For (b)–(d) $E_b=6.0$, $\langle\delta h\rangle=320$; $E_b=5.0$, $\langle\delta h\rangle=640$, and $E_b=3.0$, $\langle\delta h\rangle=5120$.

bond-breaking activation energies of $E_b=3.0$, 5.0, 6.0, and 7.0. For the higher bond-breaking activation energies [Figs. 5(a) and 5(b)], the pitting pattern was very dynamic. New pits appeared after only a small number of additional layers were removed and old pits disappeared. The total range of surface heights remained fairly constant—just a few height units (lattice units a) for $E_b=7.0$ and a range of 10–15 for $E_b=6.0$. Based on these observations, it appears likely that Figs. 5(a) and 5(b) are representative of the asymptotic (long time limit) behavior of the system. However, surface features in parts (a) and (b) are comparable with the system size, and larger scale simulations run for much longer times would be needed to evaluate this idea. Such simulations are possible, but they are not convenient on a workstation. When the activation energy is reduced to 5.0 [Fig. 5(c)] the pits grow deeper, and the surface is less dynamic. The pits become deeper as the bond-breaking activation energy decreases, and more material must be removed to erase a deeper pit. In addition, the pit cores deepen at a rate which is greater than the average rate at which the surface recedes due to dissolution, and this "stabilizes" the pits. The pattern shown in Fig. 5(c) appears to be stable under growth. However, the pattern does include features with sizes comparable to the overall system size, and if a simulation with the same parameters was carried out using a surface size greater than 2048×2048, then these features might have been larger. This trend continues when the bond-breaking activation energy is reduced to $E_b=3.0$ [Fig. 5(d)]. However, the pitting pattern is very much different in Fig. 5(d). Even after the average height has been reduced by $\delta h\geqslant 5120$ the pattern retains the

Author complimentary copy. Redistribution subject to AIP license or copyright, see http://jcp.aip.org/jcp/copyright.jsp

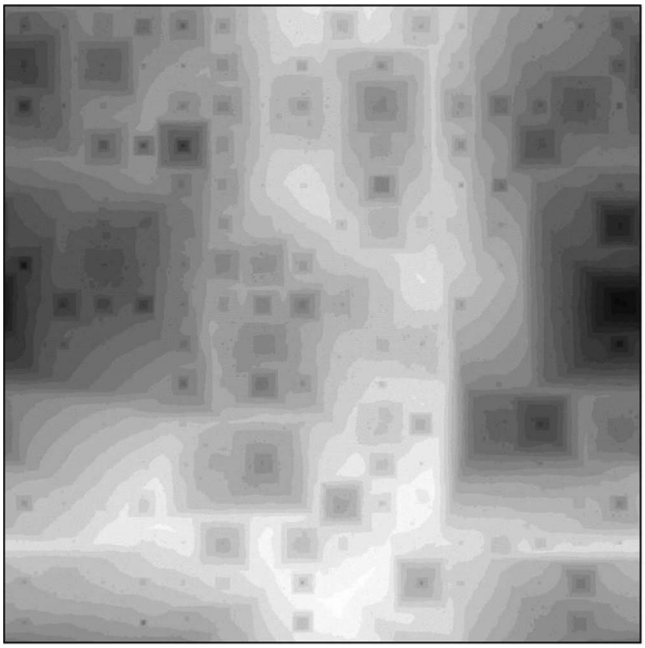

FIG. 6. A dissolving surface generated by a simulation similar to that used to generate Fig. 5(b), but with a surface of area of 4096×4096 instead of 2048×2048. The line defect density (1.53×10^{-5}) was the same in both simulations, and all other model parameters were also the same. Because Figs. 5(b) and 6 are displayed on the same scale, they can be directly compared.

full symmetry of the dislocation array on the scale and resolution used in this figure. It seems likely that this pattern is stable. It is evident from Fig. 5 that random microscopic fluctuations play an important role in the evolution of pitting patterns. The random fluctuations break the initial symmetry and the cumulative effects of the fluctuations are evidently quite large. It appears that the dissolution process amplifies the effects of the fluctuations for intermediate bond-breaking activation energies. One possible mechanism for this is that the random fluctuations (the random selection of "solid" sites for conversion to "liquid" sites in the model, with probabilities proportional to their dissolution rates) randomly deepen the pits by dissolution near their cores, and the amount of material dissolved is amplified by lateral dissolution.

To evaluate the effects of the finite system size on the simulation shown in Fig. 5(b), a similar simulation with the same dislocation density (a regular 16×16 array of dislocations) was performed on a system with a surface area of 4096×4096. The results of this simulation are shown in Fig. 6. While parts of Fig. 6 are similar to Fig. 5(b), it is clear that Fig. 6 also contained features that are of comparable scale to the overall scale of the system. This implies that still larger scale simulations may be required to completely overcome finite system size effects in this particular case.

Figure 7 shows some results from simulations carried out to investigate the effects of screw defect density on the morphology of dissolving surfaces. Simulations were carried out with Young's modulus of 1700 (twice the Young's modulus used in all of the other simulations) and a high bond-breaking activation energy ($E_b = 12.0$). The structure of the surface is shown after the mean surface height had been reduced by 500. In some cases, the surface structure after the

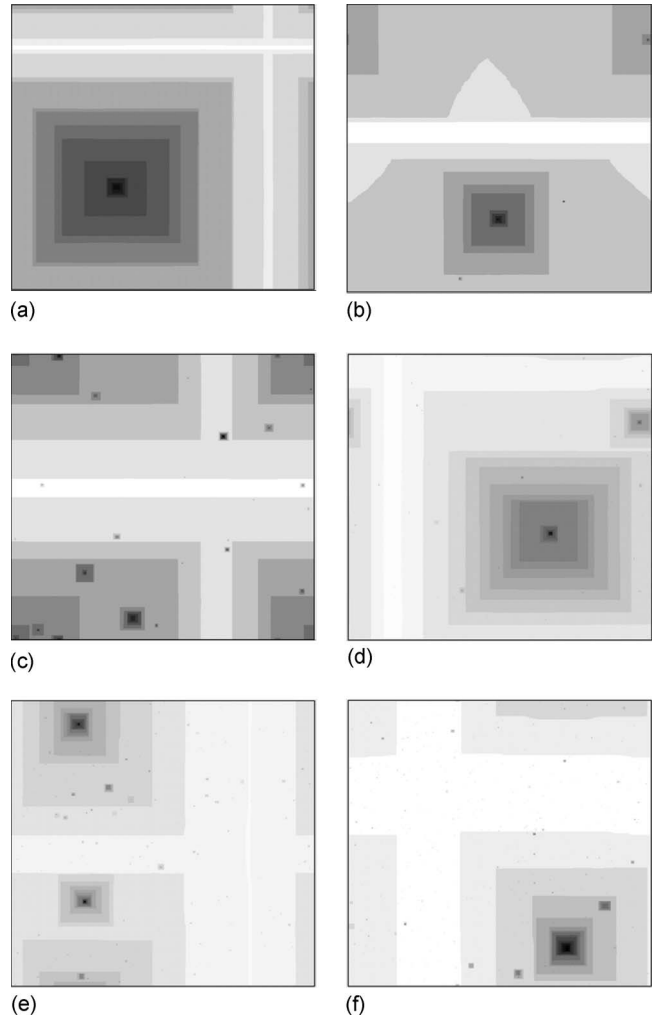

FIG. 7. Etch-pit patterns from simulations carried out with a variable number of screw dislocations with Burgers vectors of magnitude $b = 1.0$. Young's modulus of $Y_m = 1700$ and a Poisson ration of $\nu = 0.3$ were used in this simulation. A sharp strain energy density cutoff corresponding to the single dislocation strain energy density at a radius of 1.1 was used, and the bond-breaking activation energy was $E_b = 12.0$. In all cases, the etch-pit pattern is shown after the average surface height was reduced by 500. (a) shows the surface obtained with two (well separated) dislocations, but the surface contains only one pit. (b), (c), (d), (e), and (f) show the surface morphologies generated using 8, 32, 128, 512, and 2048 screw dislocations.

average height had been reduced by 100 was quite similar to the structure after the average surface height had been reduced by 500, but in other cases the two surfaces were quite different. Perhaps the most remarkable aspect of Fig. 7 is the similarity of the surfaces, irrespective of the number of underlying dislocations. In this case, it appears that the rate of overall lowering of the surface height and the rate of pit deepening at and near dislocation cores at the bottom of shallow pits are almost equal. Under the conditions of these simulations (a large bond-breaking activation energy) the rate of retreat of step edges is very fast compared with the rate at which new pits nucleate and deepen. The dominant surface lowering process is step flow and deep pits do not develop because the rate of surface retreat due to step flow dissolution keeps up with the rate of pit deepening. The simulation results suggest that random fluctuations can lead to the nucleation of a new pit, and if the new pit continues to

Author complimentary copy. Redistribution subject to AIP license or copyright, see http://jcp.aip.org/jcp/copyright.jsp

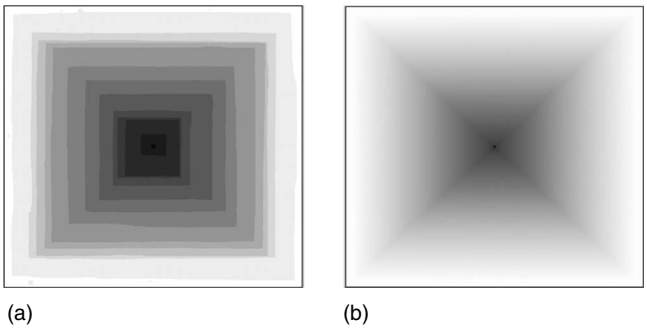

FIG. 8. Simulation of the growth of a single pit controlled by an edge dislocation. Young's modulus of 850, a Poisson ratio of $\nu=0.3$, a Burgers vector of magnitude $b=1$, and a strain energy density cutoff length of $\rho_E^{\max}=3.5$ were used in these simulations. In (a), a bond-breaking activation energy of $E_b=8.0$ was used and in (b), the bond-breaking activation energy was $E_b=4.0$. Both parts show pits formed after an average surface height has been reduced by 250. In an infinite mineral surface, the pit shown would have grown far beyond the 1024×1024 area shown here.

be favored by random fluctuations, it may deepen faster than the more established pit, which becomes shallower and eventually disappears as the average surface height decreases.

EDGE DISLOCATIONS

Since the stress and strain fields associated with edge dislocations are not invariant to rotation about the axis of the defect, they have a more complex form. All of the simulations were carried out by first adding the stress and strain fields generated by individual dislocations, then calculating the strain energy density from these summed stress and strain fields, and finally reducing the strain energy densities that exceeded a threshold value to the threshold value $\rho_E^{\max}$. The strain energy densities at the cutoff radii, corresponding to a strain of ≈0.1, were similar to those used in the point defect and screw dislocation accelerated dissolution simulations. The idea that the material in the core of a dislocation has a liquidlike structure, with a maximum strain energy approximately equal to the latent heat of fusion, suggests that the maximum strain energy density is of the order of a few k_BT, and this is consistent with cutoff strains of ≈0.1.

Figure 8 shows results from simulations of the dissolution of single pits carried out using Young's modulus of $Y_m=850$, a Poisson ratio of $\nu=0.3$ (a shear modulus modulus of $G_m=327$), a Burgers vector with magnitude $b=1$, and a cutoff of $\rho_E^{\max}=3.5$ for the strain energy. For the most part, etch pits simulated with the strain energy density field of an edge dislocation are very similar to etch pits simulated with the strain energy density field of a screw dislocation, and this is indicated by the similarities between Figs. 3 and 8. It is possible to form a pit at a higher bond-breaking activation energy for the screw dislocation [compare Figs. 3(a) and 8(a)] because the strain energy is larger for an edge dislocation (with the same Young's modulus, Poisson ratio, and Burgers vector magnitude) and the cutoff energy density of $\rho_E^{\max}=3.5$ used in the simulations that generated Fig. 8 is larger than the maximum strain energy density at the center of the screw dislocations used in the simulations illustrated in Fig. 3. The large pit shown in Fig. 8(a) lacks the small secondary pits seen in Fig. 3(a). However, this is expected

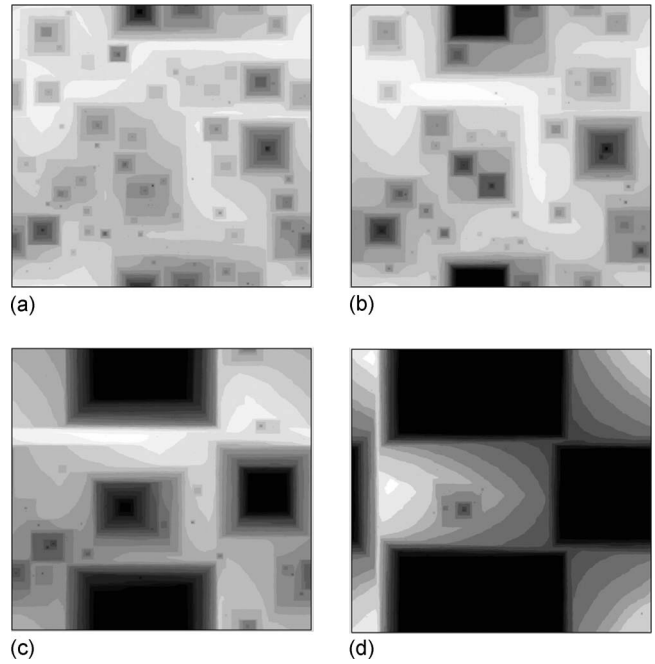

FIG. 9. Simulation of multiple etch-pit growth controlled by 100 randomly placed edge dislocations intersecting a 2024×2024 surface. Young's modulus of $Y=850$, a Poisson ration of $\nu=0.3$, and a strain energy cutoff of 3.0 were used in the simulation. The magnitude of Burger's vector was $|\mathbf{b}|=1.0$, and equal numbers of edge dislocations with Burgers vectors of $+x$, $-x$, $+y$, and $-y$ were used. The bond-breaking activation energy was set to $E_b=7.0$. (a), (b), (c), and (d) show the surface height field after the average height was reduced by 10, 20, 40, and 80. Several small, shallow pits, are located inside the large pits in (d) (below the level of the gray scale cutoff). Propagating step waves can be seen in several of the figures; they are particularly clear in (d).

since the large bond-breaking activation energy used to generate Fig. 8(a) makes it more difficult to spontaneously nucleate secondary pits, and the smaller terrace widths in the pit shown in Fig. 8(a) also make secondary pit formation less likely.

Figures 9 and 10 show some of the results from simulations of the growth of multiple pits controlled by edge dislocations. In both of these simulations the same random distribution of dislocation positions was used. Not surprisingly, the behavior of simulations with multiple edge dislocations parallels that of simulations with multiple screw dislocations. Figure 9 ($E_b=7.0$) and similar figures, not shown for $E_b=5.0$ and $E_b=6.0$, show that for relatively large bond-breaking activation energies, a single pit eventually dominates the entire dissolving surface. For smaller bond-breaking activation energies ($E_b=3.0$, Fig. 10), the surface morphology evolves in a much different way, and it may approach an essentially constant asymptotic (large time) form. The surfaces after the average surface height has been reduced by 5120 (not shown) and 10 240 (Fig. 10) are quite similar. However, the core regions continue to deepen faster than those regions of the surface that are located further from the dislocations, and the simulation results are equally consistent with the idea that the surface will continue to evolve until a single pit dominates the surface. The accumulation of the random fluctuations inherent in both the kinetic Monte Carlo simulations and natural dissolution processes may lead

Author complimentary copy. Redistribution subject to AIP license or copyright, see http://jcp.aip.org/jcp/copyright.jsp

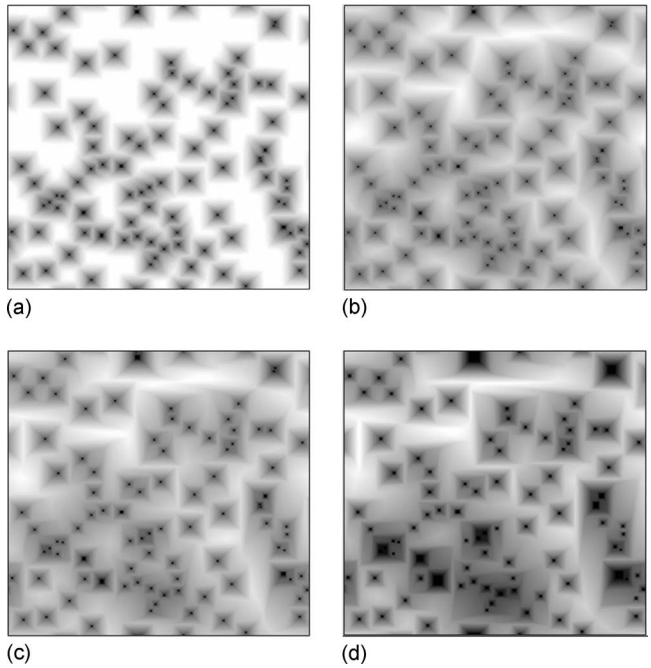

FIG. 10. Simulation of multiple etch-pit growth controlled by 100 randomly placed edge dislocations intersecting a 2024×2024 surface. Young's modulus of $Y=850$, a Poisson ration of $\nu=0.3$, and a strain energy cutoff of 3.0 were used in the simulation. The magnitude of Burger's vector was $|\mathbf{b}|=1.0$, and equal numbers of edge dislocations with Burgers vectors of $+x$, $-x$, $+y$, and $-y$ were used. The bond-breaking activation energy was set to $E_b=3.0$. (a), (b), (c), and (d) show the surface height field after the average height was reduced by 80, 640, 2560, and 10240. In (d), the gray scale covers a height range of 1200. Most of the dissolved cores extend to depths greater than 50 000 below the maximum surface height.

to a different asymptotic (long time) behavior. However, this limit will have no relevance to real line defect-mediated dissolution processes. As already mentioned, line defects are curved, they can form loops that are closed or terminate at free surfaces, and they form complex tangles.[66–69] These deviations from a model in which all the line dislocations are assumed to be straight and oriented perpendicular to the dissolving surface will have much more important consequences than the way in which the effects of random fluctuations accumulate over time.

Simplified models for line defect controlled pit growth

Under some circumstances, the effect of a line defect on etch-pit formation is dominated by the rapid dissolution of the core of the dislocation and the effect of the stress/strain field is secondary. Based on this idea, several simple models were developed. In the no strain/empty core model the core of the dislocation was removed at the start of the simulation, and the effects of the stress/strain field were ignored. Figure 11 shows examples of etch pits simulated using this model. In parts (a) and (b), the height of the surface was reduced to zero in a single site containing the lateral coordinates of the line defect, and in parts (c) and (d) the height of the surface was reduced to zero in a 3×3 block of sites at the start of the simulations. The initial height of the surface was set to a value that was large enough to ensure that surface heights of regions outside of the empty cores remained positive. The

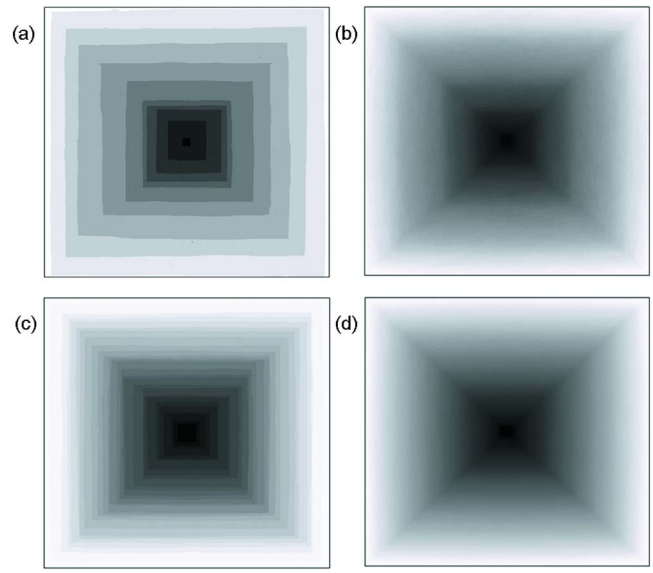

FIG. 11. (Color online) Simulation of the growth of etch pits using the no strain/empty core model. In all parts the pit formed after the average height had been reduced by 250 is shown. In an infinite mineral surface, the pit shown in (a) and (c) would have grown far beyond the 1024×1024 area shown here. (a) and (c) were obtained with a bond-breaking activation energy of $E_b=8.0$, and $E_b=4.0$ in (b) and (d). In (a) and (b) the empty cores have a size of 1×1, while in (c) and (d), the empty cores have a size of 3×3. The pit in (b) has a depth of 75, while the pit in (d) has a depth of 200.

motivation for this was not to take advantage of the greater speed of this simplified algorithm (it is only about twice as fast as the models described above that do include the effects of the stress/strain field) but, rather, to obtain a better understanding of the growth of multiple etch pits by eliminating the effects of the far field part of the stress/strain field. The etch pits shown in Fig. 11 are similar to those obtained using models that do include the effects of the far-field component of the stress/strain field for the same bond-breaking activation energies, and this can be seen by comparing Figs. 3, 8, and 11. In particular, the slopes of the pit surfaces increase with decreasing bond-breaking activation energy. The most significant differences are near the pit centers, where the stress/strain field is the largest. A comparison of Figs. 11(a) and 11(c) shows that for large bond-breaking activation energies, the pit is deeper after the average surface height has been reduced by 250 when the size of the empty core is larger. This behavior can be anticipated because sites can be removed more rapidly from the larger perimeter of the larger hollow core used in the simulation shown in Fig. 11(c). Similarly, the pit shown in Fig. 11(b) has a depth of 75, while the pit in Fig. 11(d) has a depth of 200. The ratio between the pit depths (2.66) is approximately the same as the ratio between the number of more reactive four-coordinate sites along the perimeters of the empty cores (3.0). Similar simulations were also carried out with multiple empty cores and no strain energy density effects. Figures 12 and 13 show results from simulations with 100 empty cores in an area of 2048×2048 with bond-breaking activation energies of $E_b=7.0$ and 3.0. In both simulations; and simulations with intermediate bond-breaking activation energies, the pitting pattern coarsens as material is dissolved. However, the coarsening occurs at a much earlier stage during the simulation with the

Author complimentary copy. Redistribution subject to AIP license or copyright, see http://jcp.aip.org/jcp/copyright.jsp

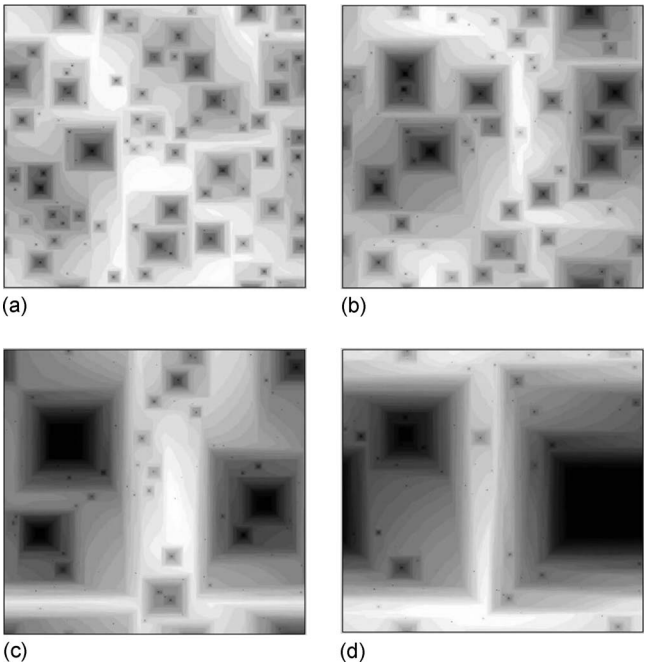

FIG. 12. Simulation of the growth of pits nucleated by 100 empty cores, each with an area of 3×3, in an area of 2048×2048. (a), (b), (c), and (d) show the surface after the average surface height has been reduced by 80, 320, 1280, and 2560. The bond-breaking activation energy is $E_b=7.0$. Like many simulations with large bond-breaking activation energies, step waves can be clearly seen on almost flat regions of the surfaces.

largest bond-breaking activation energy. In simulations with relatively large bond-breaking activation energies, the surface is dominated by just a few pits after the average surface height had been reduced by $O(10^3)$. This does not imply that the surface becomes dominated by just a few pits at an earlier *time*. The model time was not determined in these simulations, but the overall dissolution process is slower for large bond-breaking activation energies, and if the frequency factor A in Eqs. (1)–(4) is the same in both simulations, then the overall dissolution rate for $E_b=7.0$ will be approximately $e^6\approx400$ slower than the rate for $E_b=5.0$, based on the idea that the dominant dissolution process is removal of a three-coordinate site from a kink site at the edge of a terrace. Since the terrace edge density (step density) is smaller for larger bond-breaking activation energies, this is a lower limit on the actual dissolution rate ratio.

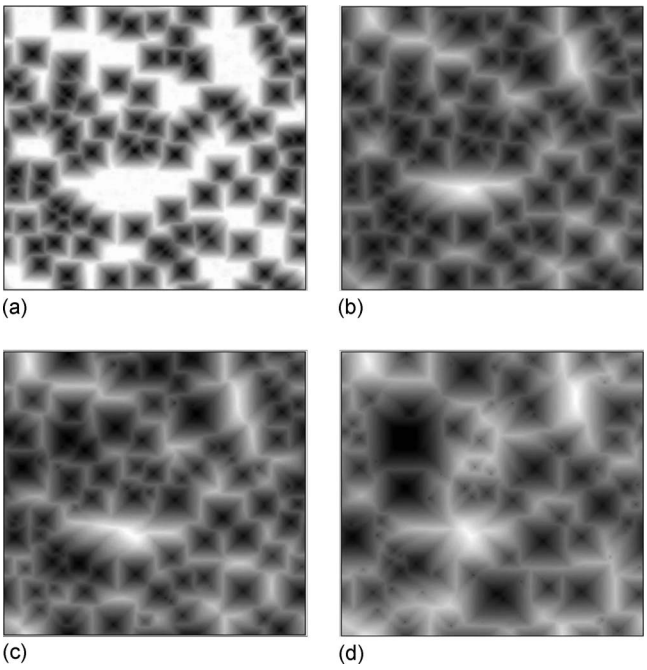

FIG. 13. Simulation of the growth of pits nucleated by 100 empty cores, each with an area of 3×3, in an area of 2048×2048. (a), (b), (c), and (d) show the surface after the average surface height has been reduced by 80, 640, 2560, and 10240. The bond-breaking activation energy is $E_b=3.0$.

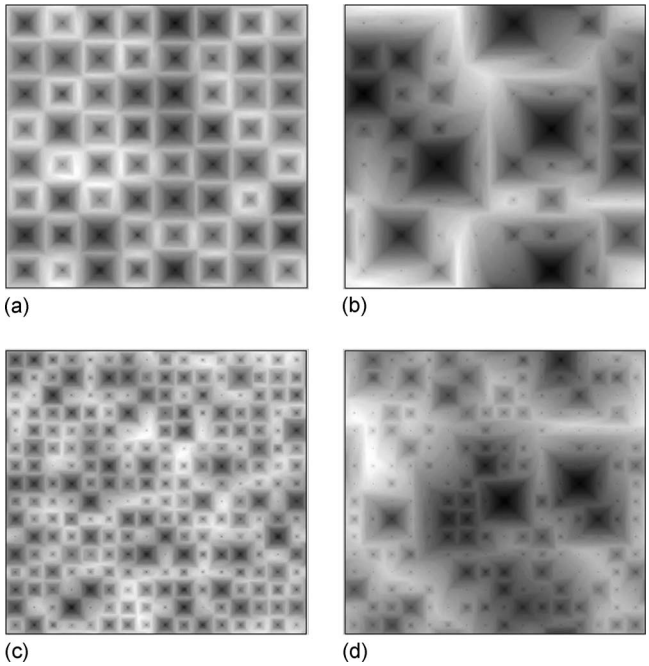

FIG. 14. Surface morphologies obtained from simulations with a regular array of empty cores. (a) and (b) show the etch-pit patterns for an array of 64 empty cores after the surface height was reduced by 320 and 10 240, while (c) and (d) show the etch-pit patterns for an array of 256 empty cores after the surface height has been reduced by 320 and 5120. In both simulations, a bond-breaking activation energy of $E_b=5.0$ was used and the empty cores consisted of vertical columns with a 3×3 cross section.

The occurrence of pit fratricide (coarsening) in the no-strain/empty-core model cannot be attributed to the growth of large pits in regions where the far-field strain energy is large, but large pits could be favored in regions in which the defect density is large. To eliminate both the far field strain energy effects and the local defect density effects, simulations were carried out using a regular array of empty cores. Figure 14 shows some of the results from simulations carried out with a regular array of empty cores, and no stress/strain fields, in an area of 2048×2048. This figure shows that the original symmetry is broken at a very early stage in the dissolution process and that the asymmetry continues to increase with increasing time. This behavior must be attributed to the effects of the fluctuations that are inherent in kinetic Monte Carlo simulations due to the random selection of events (with probabilities proportional to the local dissolution rate). The effects of these random events accumulate as time (and the number of random events) increases. The same sort of fluctuations will occur during real dissolution processes, and one of the most important attributes of kinetic

Author complimentary copy. Redistribution subject to AIP license or copyright, see http://jcp.aip.org/jcp/copyright.jsp

Monte Carlo simulations is the realistic way in which the effects of thermally driven fluctuations are included in the simulations. This can be a disadvantage if Monte Carlo simulations are used to simulate phenomena such as homogeneous chemical kinetics when the number of molecules is much too large for fluctuations to play an important role. However, the proper inclusion of fluctuations is essential to the simulation of microscopic processes, and (as these simulations demonstrate) these microscopic fluctuations can have important consequences on macroscopic phenomena.

The large effect of microscopic fluctuations on the growth of etch pits can be understood in terms of the "dissolution stepwave" concept.[23,70] According to this model, steps are generated at the core of a dislocation, and they travel outward from the dislocation because the rate of dissolution at steps is much greater than that on a flat surface, provided that the bond-breaking activation energy is large enough. A consequence of this mechanism is that nucleation of steps at the core of the defect plays a crucial role in etch-pit formation. In the simulations shown in Fig. 12, a small empty core already exists at the center of each pit. However, formation of a stepwave depends on widening of this empty core. Because relatively few dissolution events are involved in nucleation of steps at the core of the defect, the effects of microscopic fluctuations are unusually large. A closely related point of view is that growth of the pit amplifies the effects of fluctuations. The sloped surface of the pit dissolves faster than a horizontal surface because the distribution of site coordination numbers includes more low coordination number surface sites. As a pit becomes larger, its rate of mass loss becomes larger, and the effects of fluctuations that favor increased dissolution are amplified by the growth process. If the bond-breaking activation energy is small, the stepwave process will have to compete with the spontaneous nucleation and sideway growth of shallow pits, and the contrast in dissolution rates between the sloped and the horizontal surface will be less. Consequently, the mechanisms that amplify the effects of microscopic fluctuations will be reduced. This is consistent with the results shown in Figs. 9 and 10 and other simulations for both screw dislocations and edge dislocations with various bond breaking activation energies, which show that coarsening of the pitting pattern progresses more rapidly with increasing dissolution for larger bond-breaking activation energies.

These simulation results were obtained using a cubic lattice model with an initially flat {100} surface. The behavior might be quite different if the walls of the pit form a close-packed plane and/or the initial surface corresponds to a high-index plane with weak interplane bonds and/or a low bond density.

Simulations were also carried out using a "no-strain/fast core dissolution" model in which the microscopic dissolution rate in the regions representing dislocation cores was larger by a constant (coordination number independent) factor k_m. Figure 15 shows some of the results obtained from a simulation using a regular (8×8) array of cores that are more easily dissolved than the surrounding material. Although the effects of the far field stress/strain fields are omitted, the simulation was carried out using the general divide and conquer approach described above. There is a discrete number of distinct events (ten of them) in this model, but the effort of writing a new computer program to take advantage of this was not justified in view of the fact that the more general method could much more easily be modified, and the increased overhead required to handle ten discrete events would have decreased the rather small gap in speed between these two methods. If the microscopic dissolution rate k_m is small (Fig. 15), deep pits do not develop, and the only effect of the cores is the nucleation of shallow transient pits [Figs. 15(a) and 15(b)]. No substantial pits were found for average height reductions of up to $\langle \delta h\rangle = 2000$, and Fig. 15(a) shows the surface morphology after the average height had been reduced by 640. It seems very likely that this is representa-

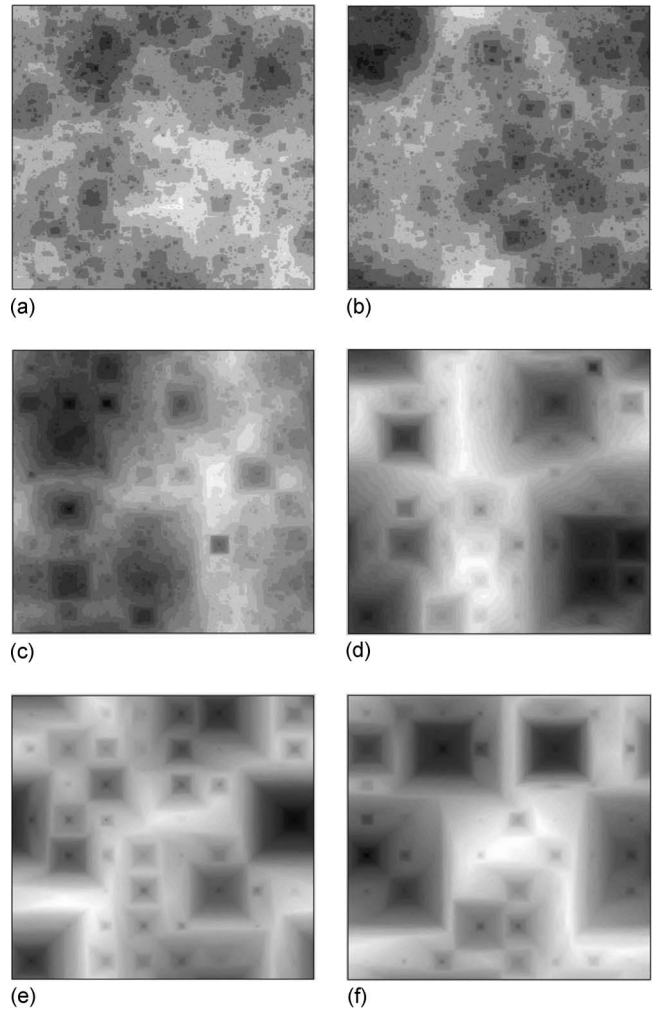

FIG. 15. Surfaces obtained from four no-strain/fast core dissolution model simulations in which the microscopic dissolution rates were larger by a factor of k_m in 64 symmetrically placed columns in a 2048×2048 surface. Each vertical column had a cross section of 3×3 (nine sites). A bond-breaking activation energy of $E_b=5.0$ was used in all of the simulations. (a) and (b) show the surface morphology obtained from a simulation with $k_m=2$ and $k_m=4$ after the average surface height has been reduced by 640. (c) ($k_m=8$, $\langle \delta h=1280\rangle$), (d) ($k_m=16$, $\langle \delta h=640\rangle$), (e) ($k_m=32$, $\langle \delta h=640\rangle$), and (f) ($k_m=32$, $\langle \delta h=5120\rangle$) show the surface morphologies obtained using larger values of k_m, which leads to pit formation. However, the total range of surface heights (the "thickness" of the surface) soon reaches an essentially constant value. The simulations indicate that the pits slowly grow and disappear as the dissolution process progresses, but the dynamics of this process becomes increasingly slower as the dissolution rate ratio k_m increases.

Author complimentary copy. Redistribution subject to AIP license or copyright, see http://jcp.aip.org/jcp/copyright.jsp

tive of the asymptotic (long time) behavior of the model. For larger values of k_m [Figs. 15(c) and 15(d)] distinct pits are formed. For $k_m=8$, the surface has a highly dynamic character. The overall character of the surface does not change after the surface height reduction has reached a small value ($O(10)$). However, new pits are formed as the surface evolves and old pits disappear. The relatively small transient pits are nucleated by the more rapidly dissolving cores, but only a small fraction of the cores have associated pits at any particular stage of development.

For larger values of k_m the pits become deeper, longer lived, and more distinct. Because some of the morphological features in Figs. 15(c)–15(f) are comparable in size to the overall system size, a simulation with $k_m=32$ was carried out on a larger scale ($L_x \times L_y = 4096 \times 4096$). The results of this simulation, not shown, indicate that the size of the morphological features do not increase with increasing system size beyond $L_x \times L_y = 2048 \times 2048$.

Similar simulations were carried out with other bond-breaking activation energies. For example, for a bond-breaking activation energy of $E_b=3.0$ and a dissolution rate ratio of $k_m=8$, the qualitative appearance of the surface and the range of surface heights quite soon became essentially constant, but new pits formed continuously as old pits disappeared. This suggests that the statistics of the surface roughness reaches a constant asymptotic limit. As the dissolution rate ratio increases, the pits become more distinct, and more material must be dissolved to reach the statistically stationary regime. For simulations with a bond-breaking activation energy of $E_b=3.0$ and dissolution rate ratios of $k_m=16$, 32, and 64, the surface morphology was still evolving after the average surface height has been reduced by $\langle \delta h = 5120 \rangle$. For $k_m=16$, hollow cores extended to a depth of about 7250, for $k_m=32$ the hollow cores are almost 12 000 deep, and for $k_m=64$ they extended to a depth of almost 29 000. During the later stages of the simulations, the evolution of the pits was quite slow. For example, in the case of the simulation with $E_b=3.0$ and $k_m=16$, the relatively broad parts of the pits (above the hollow cores) extended to depths of about 110, 125, 140, 175, and 195 for $\langle \delta h \rangle = 320$, 640, 1280, 2560, and 5120.

Simulations were also carried out with a line of oriented edge dislocations to represent dissolutions of systems with low angle grain boundaries.[26] The dissolution process results in the formation of a groove with a cross section (perpendicular to the direction of the line of dislocations) that exhibit trends similar to those observed for the cross sections of single pits formed by dissolution at a single edge dislocation as the bond-breaking activation energy is changed for the same Poisson ratio, Burgers vector, and strain energy density cutoff. As the bond-breaking activation energy is decreased the grooves become deeper and more steep walled, a line of dissolved cores extends below the groove, and these dissolved cores become deeper as the bond-breaking activation energy is reduced.

The origin of this behavior is essentially the same as that of the change in pit shapes with bond-breaking activation energy for pits dissolved around screw dislocations and edge dislocations, and it is related to the transition from dissolution step flow at high bond-breaking activation energies to the dissolution of microscopically rough surfaces at low bond-breaking activation energies. For large bond-breaking activation energies the increase in dissolution rates for solid sites at step edges (which reduces the coordination number from 5 for a site in a flat surface or the flat upper surface of a terrace to 4) and the even larger increase in dissolution rate for solid sites at kinks on step edges (which reduces the coordination number from 5 to 3) are larger than the increase in dissolution rate due the strain energy densities in and near dislocation cores, and if the bond-breaking activation energy is large enough, pit cores do not dissolve faster than the surface as a whole. On the other hand, if the surface is rough, the step flow mechanism is no longer effective and the relatively large strain energy densities at and near the dislocation cores allow a deep narrow hollow tube to develop, and this tube grows progressively deeper, relative to the dissolving surface. As the dissolved dislocation cores become progressively deeper, the rate of hollow core deepening might become diffusion limited because the concentration of solute deep in the pits could increase if solute ions cannot diffuse out of the pits rapidly enough, and the increase in the solute ion concentrations in the deepest recesses of the pit could allow the solubility product to be approached resulting in a large reduction in the dissolution rate. If the dissolved dislocation cores have very small diameters, the fluid in the cores could have properties that are significantly different from those of bulk solutions, and this could reduce (or increase) the ion diffusion coefficients.

DISCUSSION

Motivated by the desire to simulate the simultaneous growth of etch pits, we have developed computationally efficient kinetic Monte Carlo models and used them to carry out simulations in which up to 4×10^{10} surface sites are dissolved. Simulations were carried out for surface areas of up to 4096×4096 corresponding to physical scales of approximately 1×1 μm^2. This paper focuses on irreversible dissolution. However, the fast algorithms used in this work can easily be applied to and will work equally well for models that include growth and surface diffusion.

Relaxation of the strained material in the vicinity of a defect after the core has been dissolved is a potentially important issue. In the case of a point defect, this may occur when the center of the defect is dissolved, and in the case of a line defect, the surrounding material may partially relax after the core has dissolved. When a point defect is exposed, the remaining strain energy might relax completely. The simulations with screw and edge defects indicate that a very deep narrow core may form, particularly if the bond-breaking activation energy is small. However, dissolution of the core should have a relatively minor effect on the deformation of the surrounding material because the strain will be maintained by the far field displacement.

The solid-on-solid approximation is often justified by the observation that overhangs are not commonly observed during mineral dissolution. However, it could be argued that a surface site undermined by dissolution at a lower level would

Author complimentary copy. Redistribution subject to AIP license or copyright, see http://jcp.aip.org/jcp/copyright.jsp

dissolve rapidly leaving a surface with few overhangs, even though dissolution occurred beneath the upper surface. During the pit growth simulations described in this paper, almost all of the steps on the surface have a height of one lattice unit, and there is no opportunity for dissolution below the upper surface. However, large steps develop inside the deep narrow hollow cores that can develop during dissolution, and the solid-on-solid approximation might break down in this crucial region. The consequences of breakdown of the solid-on-solid approximation inside hollow pit cores will be investigated in future work.

The simple computer models described above are capable of producing a wide range of patterns. This reflects the diversity of the pitting patterns observed during the dissolution of real minerals. The diversity and complexity of the patterns generated by the computer models can be easily enhanced by adding features such as anisotropy, more complex spatial distributions of defects, and a mixture of different types of dislocations or dislocations with different Burgers vectors and orientations. Under these circumstances, accidental coincidences between simulated surface morphologies and the morphologies observed in real systems should not be taken too seriously.

The development of fast algorithms, which make it possible to carry out simulations with large surface areas and follow the dissolution process until deep pits have been formed, will allow us to investigate issues such the evolution of the pit size distribution and possible scaling behavior associated with the geometry and dynamics of the dissolving surface. It will also allow smaller scale simulations to be carried out many times to obtain more accurate information about the evolution of the shapes of individual pits and systematically explore the dependence of the model behavior on model parameters.

ACKNOWLEDGMENTS

We would like to than Jens Lothe, Center for the Physics of Geological Processes at the University of Oslo, for valuable discussions. This work was made possible by a grant from the U.S. Department of Energy, Office of Basic Energy Sciences, Geosciences Program. Pacific Northwest National Laboratory is operated by Battelle for the U.S. Department of Energy under Contract No. DE-AC06-76RLO 1830.

[1] M. T. Heald, J. Geol. **64**, 16 (1956).
[2] S. Schwarz and B. Stockhert, Tectonophysics **255**, 203 (1996).
[3] R. A. Berner and J. Schott, Am. J. Sci. **282**, 1214 (1982).
[4] M. R. Lee and I. Parsons, Geochim. Cosmochim. Acta **59**, 4465 (1995).
[5] R. A. Berner, A. C. Lasaga, and R. M. Garrels, Am. J. Sci. **283**, 641 (1983).
[6] W. D. Gunter, E. H. Perkins, and I. Hutcheon, Appl. Geochem. **15**, 1085 (2000).
[7] J. P. Kaszuba, D. R. Janecky, and M. G. Snow, Appl. Geochem. **18**, 1065 (2003).
[8] M. Akatsuka, K. Sueoka, and T. Yamamoto, J. Cryst. Growth **210**, 366 (2000).
[9] B. Dam, N. J. Koeman, J. H. Rector, B. Stauble Pumpin, U. Poppe, and R. Griessen, Physica C **261**, 1 (1996).
[10] C. T. Lin, J. Cryst. Growth **143**, 110 (1994).
[11] I. Yonenaga, T. Taishi, X. Huang, and K. Hoshikawa, J. Appl. Phys. **89**, 5788 (2001).
[12] E. K. Wheeler, R. Fluck, B. Woods, and P. K. Whitman, Appl. Opt. **42**, 5545 (2003).
[13] J. Zhou, J. E. Reddic, M. Sinha, W. S. Ricker, J. Karlinsey, J. W. Yang, M. A. Khan, and D. A. Chen, Appl. Surf. Sci. **202**, 131 (2002).
[14] M. S. Joshi, P. N. Kotru, and I. Ma, Sov. Phys. Crystallogr. **15**, 83 (1970).
[15] M. S. Joshi and A. S. Vag, Sov. Phys. Crystallogr. **12**, 573 (1968).
[16] M. W. Wegner and J. M. Christie, Contrib. Mineral. Petrol. **43**, 195 (1974).
[17] M. W. Wegner and J. M. Christie, Phys. Chem. Miner. **9**, 67 (1983).
[18] J. J. Gilman and W. G. Johnston, edited by J. C. Fisher, W. G. Johnston, R. Thomson, and T. Vreeland, *Dislocations and Mechanical Properties of Crystals* (Wiley, New York, 1957), p. 116.
[19] A. E. Blum and A. C. Lasaga, in *Aquatic Surface Chemistry: Chemical Processes at the Particle-Water Interface*, edited by W. Stumm (Wiley, New York, 1987), p. 255.
[20] N. Cabrera, M. M. Levine, and J. S. Plaskett, Phys. Rev. **96**, 1153 (1954).
[21] F. C. Frank, Acta Crystallogr. **4**, 497 (1951).
[22] A. C. Lasaga and A. E. Blum, Geochim. Cosmochim. Acta **50**, 2363 (1986).
[23] A. C. Lasaga and A. Luttge, Eur. J. Mineral. **15**, 603 (2003).
[24] M. D. Vinson and A. Luttge, Am. J. Sci. **305**, 119 (2005).
[25] S. Yanina and K. M. Rosso, Science **320**, 218 (2008).
[26] S. Yanina, K. M. Rosso, and P. Meakin, Geochim. Cosmochim. Acta **70**, 1113 (2006).
[27] A. L. Barabasi and H. E. Stanley, *Fractal Concepts in Surface Growth* (Cambridge University Press, Cambridge, 1995).
[28] W. K. Burton, N. Cabrera, and F. C. Frank, Philos. Trans. R. Soc. London, Ser. A **243**, 299 (1951).
[29] G. H. Gilmer, Science **208**, 355 (1980).
[30] P. Meakin, *Fractals, Scaling and Growth Far from Equilibrium* (Cambridge University Press, Cambridge, 1998).
[31] J. M. McCoy and J. P. LaFemina, Surf. Sci. **373**, 288 (1997).
[32] A. J. Gratz and P. Bird, Geochim. Cosmochim. Acta **57**, 965 (1993).
[33] J. W. Tester, W. G. Worley, B. A. Robinson, C. O. Grigsby, and J. L. Feerer, Geochim. Cosmochim. Acta **58**, 2407 (1994).
[34] W. G. Worley, J. W. Tester, and C. O. Grigsby, AIChE J. **42**, 3442 (1996).
[35] M. S. Paterson, Rev. Geophys. **11**, 355 (1973).
[36] R. Raj and C. K. Chyung, Acta Metall. **29**, 159 (1981).
[37] E. H. Rutter, Philos. Trans. R. Soc. London, Ser. A **283**, 203 (1976).
[38] P. K. Weyl, J. Geophys. Res. **64**, 2001 (1959).
[39] M. D. Johnson, C. Orme, A. W. Hunt, D. Graff, J. Sudijono, L. M. Sander, and B. G. Orr, Phys. Rev. Lett. **72**, 116 (1994).
[40] M. I. Larsson, R. F. Sabiryanov, K. Cho, and B. Clemens, J. Appl. Phys. **94**, 3470 (2003).
[41] J. M. Burgers, Proc. K. Ned. Akad. Wet. **42**, 293 (1939).
[42] R. B. Hetnarski and J. Ignaczak, *Mathematical Theory of Elasticity* (Taylor and Francis, London, 2004).
[43] J. P. Hirth and J. Lothe, *Theory of Dislocations*, 2nd ed. (Wiley, New York, 1982).
[44] D. Hull and D. J. Bacob, *Introduction to Dislocations*, 4th ed. (Butterworth-Heinemann, Oxford, 2001).
[45] S. D. Piersall and J. B. Anderson, J. Chem. Phys. **95**, 971 (1991).
[46] T. Vicsek and F. Family, Phys. Rev. Lett. **52**, 1669 (1984).
[47] C. C. Battaile and D. J. Srolovitz, Annu. Rev. Mater. Res. **32**, 297 (2002).
[48] R. Weinkamer, P. Fratzl, H. S. Gupta, O. Penrose, and J. L. Lebowitz, Phase Transitions **77**, 433 (2004).
[49] S. M. Auerbach and H. I. Metiu, J. Chem. Phys. **105**, 3753 (1996).
[50] M. J. Caturla, Comput. Mater. Sci. **12**, 319 (1998).
[51] R. M. Ziff, E. Gulari, and Y. Barshad, Phys. Rev. Lett. **56**, 2553 (1986).
[52] A. Saul, G. Treglia, and B. Legrand, Surf. Sci. **307**, 804 (1994).
[53] E. van Veendaal, P. van Buerden, W. J. P. van Enkevort, and E. Vlieg, J. Appl. Phys. **88**, 4595 (2000).
[54] M. Belhadj, H. E. Alper, and R. M. Levy, Chem. Phys. Lett. **179**, 13 (1991).
[55] M. Y. Frenkel and E. A. Wasserman, Geokhimiya (8), 1194 (1991).
[56] J. Hautman and M. L. Klein, Mol. Phys. **75**, 379 (1992).
[57] Y. J. Rhee, J. W. Halley, J. Hautman, and A. Rahman, Phys. Rev. B **40**, 36 (1989).
[58] D. Bratko and D. Henderson, Phys. Rev. E **49**, 4140 (1994).
[59] L. L. Lee, M. Llano Restrepo, W. G. Chapman, and K. P. Shukla, J. Chin. Inst. Chem. Eng. **27**, 213 (1996).
[60] A. P. Lyubartsev and L. Nordenskiold, J. Phys. Chem. **99**, 10373 (1995).

Author complimentary copy. Redistribution subject to AIP license or copyright, see http://jcp.aip.org/jcp/copyright.jsp

[61] H. J. Strauch and P. T. Cummings, Fluid Phase Equilib. **83**, 213 (1993).
[62] P. P. Ewald, Ann. Phys. **64**, 253 (1921).
[63] N. Metropolis, A. W. Rosenbluth, M. N. Rosenbluth, A. H. Teller, and E. Teller, J. Chem. Phys. **21**, 1087 (1953).
[64] P. A. Maksym, Semicond. Sci. Technol. **3**, 594 (1988).
[65] D. Kuhlmann-Wilsdorf, Phys. Rev. **140**, A1599 (1965).
[66] P. Hahner, K. Bay, and M. Zaiser, Phys. Rev. Lett. **81**, 2470 (1998).
[67] F. Szekely, I. Groma, and J. Lendvai, Mater. Sci. Eng., A **309**, 352 (2001).
[68] F. Szekely, I. Groma, and J. Lendvai, Mater. Sci. Eng., A **324**, 179 (2002).
[69] J. Weiss and D. Marsan, Science **299**, 89 (2003).
[70] A. Luttge, U. Winkler, and A. C. Lasaga, Geochim. Cosmochim. Acta **67**, 1099 (2003).

Author complimentary copy. Redistribution subject to AIP license or copyright, see http://jcp.aip.org/jcp/copyright.jsp